High and Variable Drag in a Sinuous Estuary With Intermittent Stratification

Bo, Tong; Ralston, David K.; Kranenburg, Wouter M.; Geyer, W. Rockwell; Traykovski, Peter

DOI
10.1029/2021JC017327

Publication date
2021

Document Version
Final published version

Published in
Journal of Geophysical Research: Oceans

Citation (APA)
Bo, T., Ralston, D. K., Kranenburg, W. M., Geyer, W. R., & Traykovski, P. (2021). High and Variable Drag in a Sinuous Estuary With Intermittent Stratification. *Journal of Geophysical Research: Oceans*, *126*(10), Article e2021JC017327. https://doi.org/10.1029/2021JC017327

ADVANCING EARTH AND SPACE SCIENCE

JGR Oceans

RESEARCH ARTICLE
10.1029/2021JC017327

High and Variable Drag in a Sinuous Estuary With Intermittent Stratification

Tong Bo[1,2], David K. Ralston[1], Wouter M. Kranenburg[1,3,4], W. Rockwell Geyer[1], and Peter Traykovski[1]

[1]Applied Ocean Physics and Engineering Department, Woods Hole Oceanographic Institution, Woods Hole, MA, USA, [2]MIT-WHOI Joint Program, Cambridge, MA, USA, [3]Deltares, Marine and Coastal Systems, Delft, The Netherlands, [4]Department of Hydraulic Engineering, Delft University of Technology, Delft, The Netherlands

Key Points:

- The drag in a sinuous estuary is greater than expected from bottom friction alone, and it varies at tidal and seasonal time scales
- Form drag due to flow separation at sharp bends can explain the high drag and its tidal asymmetry
- Overbank flow and stratification may inhibit flow separation and decrease the associated form drag

Correspondence to:

T. Bo,
tongbo@mit.edu

Citation:

Bo, T., Ralston, D. K., Kranenburg, W. M., Geyer, W. R., & Traykovski, P. (2021). High and variable drag in a sinuous estuary with intermittent stratification. *Journal of Geophysical Research: Oceans*, *126*, e2021JC017327. https://doi.org/10.1029/2021JC017327

Received 2 MAR 2021
Accepted 27 SEP 2021

Abstract

In field observations from a sinuous estuary, the drag coefficient C_D based on the momentum balance was in the range of $5-20 \times 10^{-3}$, much greater than expected from bottom friction alone. C_D also varied at tidal and seasonal timescales. C_D was greater during flood tides than ebbs, most notably during spring tides. The ebb tide C_D was negatively correlated with river discharge, while the flood tide C_D showed no dependence on discharge. The large values of C_D are explained by form drag from flow separation at sharp channel bends. Greater water depths during flood tides corresponded with increased values of C_D, consistent with the expected depth dependence for flow separation, as flow separation becomes stronger in deeper water. Additionally, the strength of the adverse pressure gradient downstream of the bend apex, which is indicative of flow separation, correlated with C_D during flood tides. While C_D generally increased with water depth, C_D decreased for the highest water levels that corresponded with overbank flow. The decrease in C_D may be due to the inhibition of flow separation with flow over the vegetated marsh. The dependence of C_D during ebbs on discharge corresponds with the inhibition of flow separation by a favoring baroclinic pressure gradient that is locally generated at the bend apex due to curvature-induced secondary circulation. This effect increases with stratification, which increases with discharge. Additional factors may contribute to the high drag, including secondary circulation, multiple scales of bedforms, and shallow shoals, but the observations suggest that flow separation is the primary source.

Plain Language Summary

In shallow estuaries, bottom roughness is usually a major contribution to the flow resistance. The drag coefficient C_D is a dimensionless number that is typically used to quantify the overall flow resistance. In field observations from a sinuous estuary, C_D was much greater than expected from bottom roughness alone. We find that sharp bends in the channel lead to flow separation and recirculating eddies, and this creates "form drag" that removes energy from the flow. Our analysis links the increased C_D to the evidence of flow separation and also explains tidal and seasonal variations in C_D. This observational study suggests that channel curvature can greatly increase flow resistance and affect the tidal dynamics in similar estuaries.

1. Introduction

The drag force is an important part of the estuarine momentum balance, and it directly affects tidal propagation, flooding potential, and marsh inundation as well as estuarine exchange, mixing processes, and salinity intrusion (e.g., Geyer, 2010). Models to predict water level elevations and velocities in estuaries require appropriate parameterization of the drag (e.g., Lewis & Lewis, 1987). The drag coefficient C_D is one of the typical ways to quantify the drag and is defined as

$$C_D = \frac{\tau}{\rho U\,|U|}, \tag{1}$$

where τ is the total drag, ρ is density, and U is a reference velocity, usually taken at a fixed elevation (e.g., 1 m above the bed) or as the depth average.

Drag in shallow flows (e.g., estuaries, rivers, and the coastal ocean) is mainly attributed to bottom friction. A common value for C_D used in estuaries and tidal channels is around 3×10^{-3} (e.g., Dronkers, 1964; Geyer et al., 2000; Sternberg, 1968; Soulsby, 1990), but C_D can vary depending on the dominant sources of drag. C_D

due to bottom roughness can be calculated directly by assuming a near-bed boundary layer velocity profile (e.g., Gross et al., 1999; Lentz et al., 2017). The bottom friction also depends on the size and structure of roughness elements like bedforms (Fong et al., 2009; Grant & Madsen, 1982) and can be enhanced by wind waves (Bricker et al., 2005; Grant & Madsen, 1986). Factors other than bottom friction can also contribute to the drag, for example, stem drag from vegetation (e.g., Kadlec, 1990; Nepf, 1999) and form drag from large topographic features, including headlands (McCabe et al., 2006) and channel bends (Seim et al., 2006).

A sinuous channel planform is a common feature of many estuaries (Marani et al., 2002) and the channel curvature influences the flow structure and the drag (e.g., Lacy & Monismith, 2001; Leeder & Bridges, 1975; Seim et al., 2006). Increased flow resistance due to channel curvature has been examined extensively in rivers and laboratory channels (e.g., Arcement & Schneider, 1989; Chang, 1984; Chow, 1959; Leopold, 1960). Several processes have been identified as contributing to increased drag in sinuous channels, including secondary circulation (e.g., Chang, 1984) and flow separation (e.g., Leopold, 1960).

Secondary circulation due to flow curvature interacts with the primary along-channel flow to increase drag. Flow around a bend generates a water level setup near the outer bank and a setdown near the inner bank (Kalkwijk & Booij, 1986; Thomson, 1877). This lateral water level slope yields a barotropic pressure gradient that balances the centrifugal acceleration. Vertical shear in the streamwise flow causes a depth-dependent imbalance between these two forcing terms and, as a result, secondary circulation develops in the lateral plane perpendicular to the primary flow direction. In estuaries, lateral baroclinic pressure gradients caused by salinity variation can also affect the secondary circulation in bends (e.g., Kranenburg et al., 2019; Nidzieko et al., 2009; Pein et al., 2018). Laboratory experiments have shown that secondary circulation can increase drag by: (a) increasing the lateral velocity and creating an additional bed shear stress component; (b) vertically advecting high momentum toward the channel bed, compressing the bottom boundary layer, and increasing the bottom stress (Blanckaert & de Vriend, 2003; Blanckaert & Graf, 2004; Chang, 1983). In observations from estuaries, secondary circulation associated with channel curvature has been found to increase turbulent stresses and the drag (Fong et al., 2009; Seim et al., 2002).

In addition to secondary circulation, drag can be enhanced due to flow separation and the associated form drag at channel bends. Channel curvature creates a lateral water level slope in the bend, and as the curvature effect decreases downstream from the bend apex, the lateral water level slope decreases toward the exit of the bend. As a result, an adverse pressure gradient can occur along the inner bank potentially causing flow separation (Blanckaert, 2010; Vermeulen et al., 2015). With flow separation, streamlines of the main flow detach from the inner bank and recirculating lee eddies are generated (Leeder & Bridges, 1975; Leopold, 1960). The separation zone has a lower water surface elevation than the main flow, and the resulting pressure difference around the bend creates form drag that can be a major contribution to the total drag (Bo & Ralston, 2020; McCabe et al., 2006). The drag associated with flow separation has been studied in laboratory experiments with unidirectional flow (e.g., James et al., 2001; Leopold, 1960), and Bo and Ralston (2020) conducted numerical model studies to investigate form drag and explain its parameter dependence in curved estuarine flows with idealized channels.

In this research, we calculate from observations the drag coefficient in an estuary with channel curvature and intermittent stratification, and investigate factors potentially contributing to the observed drag coefficients that are greater than expected from bottom roughness alone. In Section 2, we introduce the field site, measurements, and data processing methods. The calculated drag coefficient and its dependence on tides and river discharge are shown in Section 3. In Section 4, we examine factors contributing to the increased drag, including evidence of flow separation and form drag at bends, dependence on overbank flow, and the influence of stratification. In Section 5, we explain the increased drag and its variability and discuss other potential contributors. Section 6 presents conclusions.

2. Methods

2.1. Field Site

The field study was conducted in the North River estuary (Massachusetts, USA), a narrow, sinuous channel through a salt marsh (Figure 1a). The tidal range of the North River varies between 2 and 3.5 m. Intertidal marshes are widespread over the banks and are inundated during high spring tides. The North River

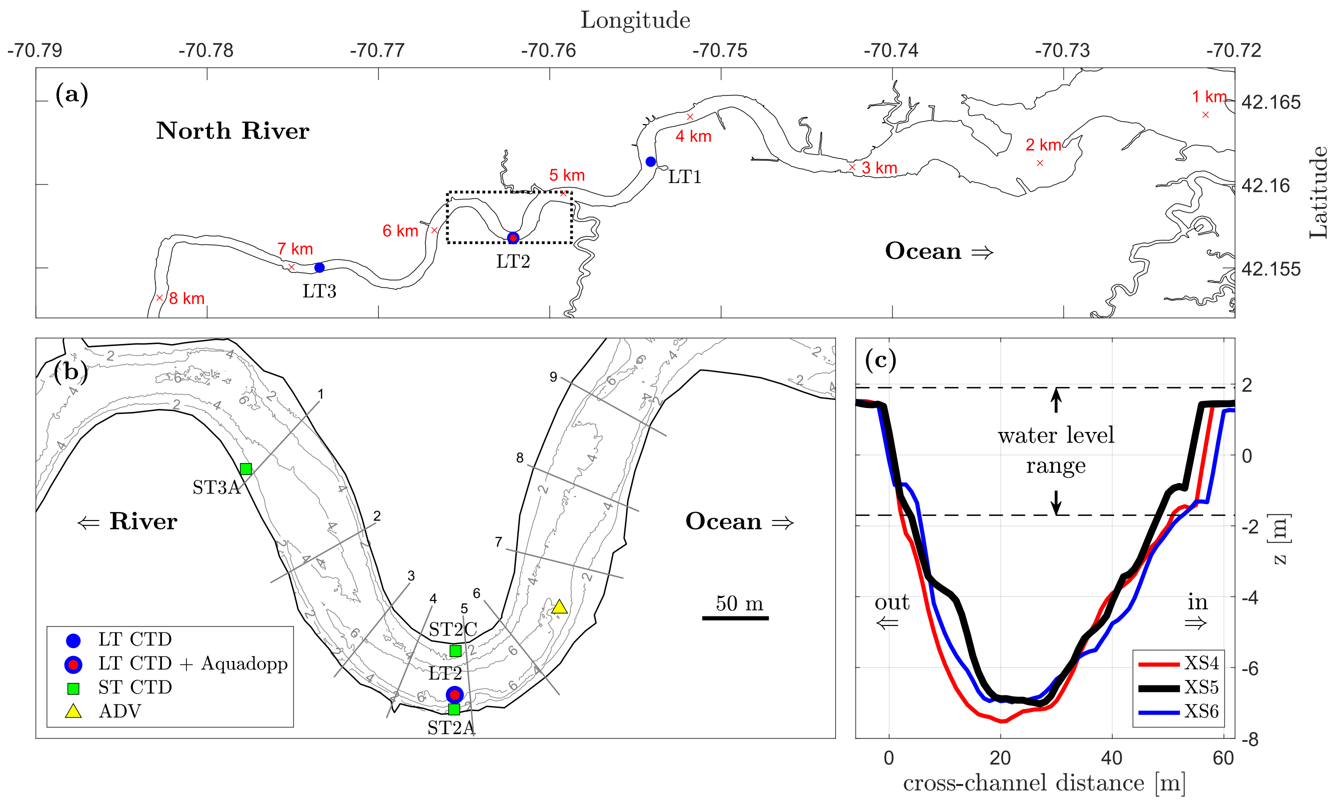

Figure 1. (a): The North River estuary, with the intensive study area marked by the rectangle. Red crosses mark the along-channel distance from the mouth. (b): The intensive study area with contours showing the bathymetry, with locations of long-term (LT) conductivity-temperature-depth (CTD) sensors, short-term (ST) CTD sensors, Aquadopp profiler, and acoustic Doppler velocimeter (ADV) measurements. Gray lines represent shipboard survey transects. (c): Three cross-sectional profiles near the bend apex that correspond to transects 4, 5, and 6 in (b). The two dashed lines show the tidal water level range and z = 0 is the mean water level.

has a modest discharge, based on USGS discharge measurements in a contributory stream upriver (station 01105730) that have been scaled up according to the total catchment area (Kranenburg et al., 2019). During the high-flow season of the spring, the discharge is typically 5–10 m^3/s (corresponding to a mean velocity of 2–4 cm/s in the mid-estuary) with increases of up to 30 m^3/s for rain-event peaks. In the low-flow season of summer, discharge is typically less than 5 m^3/s. The North River estuary is intermittently stratified with seasonal variation that is examined in Section 3.1.

The focus of this study is in the midestuary, centered around a sharp bend at about 5.4 km from the mouth of the estuary. The midestuary channel has a typical width W of about 50 m and average depth H of about 5 m, that is., an aspect ratio $W/H \approx 10$, which is common for salt marsh meanders (Marani et al., 2002). At the apex of the sharp bend that was the focus of the observations, the radius of curvature is $R \approx 60$ m, yielding a curvature ratio $R/W \approx 1.2$. Most other midestuary bends are less sharp, with a radius of curvature of around 100–200 m and R/W of 2–4. The range of R/W in the North River is representative of the bend sharpness generally found in sinuous rivers (Leopold & Wolman, 1960) and tidal channels (Marani et al., 2002), where R/W values are typically in the range of 1.5–5 and sharp bends can have R/W of around 1 (e.g., Marani et al., 2002; Nanson, 2010; Schnauder & Sukhodolov, 2012). The cross-sectional profile at the sharp bend apex is approximately symmetric laterally, with relatively steep banks and no distinct point bar (Figure 1c). Shallow shoals exist along the inner bank on the seaward side of the sharp bend and also on the seaward side of the inner bank of the next bend landward.

Kranenburg et al. (2019) investigated the lateral circulation patterns at the apex of the sharp bend. The "normal" helical circulation for flow around a bend was observed during ebb tide, with inward flow near the bottom and outward flow near the surface. However, during flood tide, lateral circulation was reversed from the "normal" structure, with flow toward the inner bank near the surface and toward the outer bank in the lower layer. During both flood and ebb, streamwise velocity was greatest near the inner bank, which is consistent with potential flow due to curvature and indicates that friction does not play as big a role in shifting the velocity maximum toward the outer bank as is found in many river and laboratory meanders (e.g., Blanckaert, 2015; Jamieson et al., 2013). The lateral shear in the streamwise velocity creates lateral salinity differences through differential advection of the along-estuary salinity gradient. During ebbs, the lateral baroclinic pressure gradient reinforces the "normal" lateral circulation, but during flood tides the lateral baroclinic forcing is outward and counteracts the inward barotropic pressure gradient (Kranenburg et al., 2019). Triggered by this lateral baroclinic forcing, the sense of secondary circulation can therefore be reversed during flood tide.

2.2. Measurements

The field measurements used in this study overlap with those from Kranenburg et al. (2019), including time series of velocity, pressure, and salinity from April 4 to July 31 in 2017 (long-term (LT) moorings). While Kranenburg et al. (2019) investigated the lateral momentum balance and the resulting secondary circulation in the sharp bend, this study examines the drag that leads to along-channel momentum loss in the sinuous North River estuary. Pressure and salinity were measured at three mooring locations by conductivity-temperature-depth (CTD) sensors sampled every 2 min: one mooring at the bend apex (LT2) and two at comparable distances down-estuary (LT1) and up-estuary (LT3) of the bend, that is, 4.4, 5.4, and 6.9 km from the mouth, respectively (Figure 1a). Five CT/CTD sensors were deployed at LT2 with similar vertical spacing through the water column, and two CT/CTD sensors were deployed near the surface and bed at each of LT1 and LT3. The sensors nearest to the surface only measured conductivity and temperature. Velocity profile data were collected at the bend apex (same location as the LT2 CTD, about 15 m from the outer bank, Figure 1) by an upward-looking Aquadopp profiler (0.2-m vertical resolution, 10-min sample interval, and 45-s averaging period) mounted on a bottom frame. The accuracy of water depth measurement is 0.01 m, and the accuracy of Aquadopp velocity measurement is 0.005 m/s. In addition, short-term (ST) CTD sensors were deployed at the inner (ST2C) and outer (ST2A) bank of the bend apex and at the south side of the up-estuary exit of the bend (ST3A) from April 18 to May 24 (Figure 1b). Short-term CTDs were also deployed near the inner bank landward of the bend and near both banks seaward of the bend, but these deployments failed. Shipboard surveys were conducted on April 18, 19, and 27, May 17, and July 24, 25, 28, and 31 with an acoustic Doppler current profiler (ADCP, cell size 0.50 m, and profile interval 0.25 s) over cross-sections 1–9 through the bend and temperature-salinity profile measurements at lateral cross-sections 1, 3, 5, 7, and 9 (Figure 1b). An acoustic Doppler velocimeter (ADV) was deployed near the bend apex (Figure 1b) from July 24 to July 27 in 2017 for high-frequency velocity measurement (16-Hz sample rate and 12-min bursts) at about 0.5 m above the bed.

Bathymetric surveys of the study site were conducted using a Jetyak Unmanned Surface Vehicle (Kimball et al., 2014). The Jetyak was equipped with a bathymetric sidescan sonar and a post-processing kinematic global navigation system sensor coupled to an inertial motion sensor for attitude heading reference and position measurements. The bathymetric sonar is optimized for shallow water surveys and is capable of measuring seafloor topography with resolution and accuracy of better than 10 cm in both lateral and vertical dimensions in swath widths of up to ten times the water depth. The final bathymetric output was gridded in 50-cm bins for overall bathymetry of the midestuary region (Figure 1), and selected areas were gridded at 20 cm for detailed analysis of bedform geometry.

2.3. Data Analysis

We calculated the drag in the North River estuary using multiple approaches. First, the drag coefficient C_D was calculated from the depth-averaged along-estuary momentum balance, and it represents the total momentum loss in the observation region. The along-estuary momentum balance includes the along-estuary time-mean water level gradient, which is not measured directly but is estimated from theory and forcing conditions. In addition, we estimated the drag coefficient $C_{D,energy}$ using the tidal energy flux balance since drag causes energy dissipation. In addition to these larger-scale estimates of the total drag, the bottom friction coefficient C_f was calculated from local high-frequency velocity measurements and reflects the near-bed shear stress.

2.3.1. Drag Coefficient From the Momentum Balance

An approximate depth-averaged along-estuary momentum equation is

$$\frac{\partial U}{\partial t} = -g\frac{\partial \eta}{\partial s} - \frac{1}{2}\beta g\frac{\partial \langle S\rangle}{\partial s}H - \frac{C_D U\ |U|}{H}, \tag{2}$$

where we have neglected the advection and Coriolis terms. While advection can be a significant contributor to the local momentum balance in the bends, the advection term is less important when assessing the momentum budget at larger scales. η is the water level, $\langle S\rangle$ is the depth-averaged salinity, and H is the water depth. s is the along-channel coordinate and β is the haline contraction coefficient. C_D is the drag coefficient used to represent the total flow resistance including bottom friction and other sources of drag. In this analysis, C_D is defined based on the depth averaged streamwise velocity U.

We can therefore calculate a drag coefficient that satisfies the momentum budget in the North River estuary using

$$C_D = \left(\frac{\partial U}{\partial t} + g\frac{\partial \eta}{\partial s} + \frac{1}{2}\beta g\frac{\partial \langle S\rangle}{\partial s}H\right) / \left(\frac{-U\ |U|}{H}\right). \tag{3}$$

U was measured by the Aquadopp profiler at the bend apex, and calculated as the vertical average of the velocity profile. The velocity has been extrapolated in the near-bed (0.4 m) and near-surface (~0.8 m) regions that are not covered by Aquadopp measurements due to the mount height, blanking distance, and surface interference. The tidal water level gradient and salinity gradient were calculated using LT1 and LT3 CTD measurements down- and up-estuary of the bend based on the centered difference. In addition, the measured tidal water level gradient was adjusted to account for the time-mean along-estuary water level gradient that could not be assessed directly with the measurements (further explained in Section 2.3.2). H is the laterally averaged water depth, with the time series of the single-location water depth recorded by the LT2 CTD at the apex and converted to a lateral average using data from shipboard cross-channel surveys. Average depth H is calculated for the channel width and does not include the marsh extent for periods with overbank flow.

The drag term is quadratic with velocity and velocity is in the denominator of Equation 3, and therefore we focus on the averaged C_D over 1-h windows around maximum flood and ebb tide to reduce the sensitivity to low velocity periods. The calculated C_D applies to the total momentum loss at the scale of the spacing between the pressure sensors (~2.5 km) in the mid-estuary region that contains the sharp studied bend as well as several other bends that are less sharp.

2.3.2. Mean Along-Estuary Barotropic Pressure Gradient

The measured instantaneous water level at each location is the free surface deviation from the local mean water level, that is, $\eta' = h - \overline{h}$, where h is the instantaneous depth measured by CTD sensors and $\overline{h}$ is the time-mean depth. The time-mean depth is calculated using a low-pass filter over 33 h to allow for longer term variation in the measurements that do not reflect the tidal dynamics (e.g., instrument drift or movement). The measured water levels are not referenced to an absolute vertical coordinate, and to obtain the absolute water level, the measured instantaneous water level η' must be corrected as

$$\eta = \eta' + \overline{\eta}, \tag{4}$$

where η is the absolute water level and $\overline{\eta}$ is the time-mean water level (varying at subtidal timescales) that was not directly resolved in the North River observations. The calculation of C_D was based on measurements of the instantaneous water level gradient in the along-estuary momentum balance, with the absolute water level gradient forcing being

$$g\frac{\partial \eta}{\partial s} = g\frac{\partial \eta'}{\partial s} + g\frac{\partial \overline{\eta}}{\partial s}. \tag{5}$$

The first term on the right side is the measured water level gradient forcing calculated between LT1 and LT3 CTDs. The second term is the unresolved time-varying mean (subtidal) water level gradient forcing that needs to be incorporated into the momentum balance.

A mean along-estuary water level gradient can be generated due to river inputs or by tidal processes, and is typically a water level setup from seaward to landward. In the mean along-estuary momentum balance, the mean water level gradient forcing (barotropic pressure gradient, BTPG) is balanced with three forcing terms (Appendix A): the bottom friction from the mean flow, the tidal stress (e.g., Nihoul & Ronday, 1975), and the mean salinity gradient forcing (baroclinic pressure gradient, BCPG).

The bottom friction from the mean flow is estimated as (e.g., Nihoul & Ronday, 1975; Parker, 2007)

$$\tau_{b,\bar{u}} = -\frac{4}{\pi} C_f \rho \left\| U \right\| \bar{U}, \tag{6}$$

where C_f is the bottom friction coefficient, $\left\| U \right\|$ is the norm of tidal velocity, that is, the amplitude of the periodic velocity, and $\bar{U}$ is the mean flow or residual current. $\bar{U}$ is typically seaward in the estuary and is dominated by the freshwater discharge but also includes the Eulerian return flow of the landward Stokes drift of the tidal forcing (Uncles & Jordan, 1980; Zimmerman, 1979). $\bar{U}$ and $\left\| U \right\|$ were calculated from the depth averaged velocity measurements by the LT Aquadopp profiler at the bend apex (Section 2.2). C_f was set as 3×10^{-3}, a typical value for bottom friction that is consistent with the ADV measurements (Section 3.4).

The tidal stress is estimated as (e.g., Nihoul & Ronday, 1975; Zimmerman, 1978)

$$\tau_t = -\frac{1}{4} \rho g \frac{\partial}{\partial s} \left(\left\| \eta \right\|^2 \right), \tag{7}$$

where $\left\| \eta \right\|$ is the norm of tidal water level fluctuation, that is, tidal amplitude. Details of the derivation are in Appendix A. τ_t is a manifestation of the radiation stress in a tidal wave (Zimmerman, 1978) and is in the direction of tidal amplitude decay. The tidal amplitude decay was calculated between the down-estuary (LT1) and up-estuary (LT3) moorings.

The mean depth-averaged BCPG (salinity gradient forcing) was calculated using

$$\text{mean BCPG} = -\overline{\frac{1}{2} \beta g \frac{\partial \langle S \rangle}{\partial s} H}, \tag{8}$$

where the salinity gradient was estimated between LT1 and LT3 CTDs and the overbar means time averaged (low-pass filtered results).

We can estimate the mean BTPG on the North River estuary from the mean momentum balance by calculating the mean flow bottom friction, the tidal stress, and the mean BCPG, that is,

$$g \frac{\partial \bar{\eta}}{\partial s} = \frac{1}{\rho \bar{H}} (\tau_{b,\bar{u}} + \tau_t) - \overline{\frac{1}{2} \beta g \frac{\partial \langle S \rangle}{\partial s} H}, \tag{9}$$

where $\bar{H}$ is the mean water depth (low-pass filtered H measured by the LT2 CTD). The absolute BTPG can therefore be calculated by substituting Equation 9 into Equation 5

$$g \frac{\partial \eta}{\partial s} = g \frac{\partial \eta'}{\partial s} + \frac{1}{\rho \bar{H}} (\tau_{b,\bar{u}} + \tau_t) - \overline{\frac{1}{2} \beta g \frac{\partial \langle S \rangle}{\partial s} H}. \tag{10}$$

2.3.3. Drag Coefficient From the Energy Flux Balance

The second method to calculate the drag is based on the tidal energy budget. The energy flux balance for the depth-integrated tidal flow is (van Rijn, 2011)

$$\frac{\partial \left\| \eta \right\|}{\partial s} = 0.5(\gamma_w + \gamma_h) \left\| \eta \right\| - \frac{4 C_D \left\| U \right\|^2}{3 \pi g \bar{H} \cos(\Delta \phi)}, \tag{11}$$

where $\left\| \eta \right\|$ is tidal amplitude and $\left\| U \right\|$ is the amplitude of tidal velocity. $\Delta \phi$ is the phase difference between tidal water level and velocity. γ_w and γ_h are the convergence coefficients for channel width and depth.

$$\gamma_w = \frac{1}{L_w}, \gamma_h = \frac{1}{L_h}, \tag{12}$$

with L_w and L_h being the e-folding scales for channel width and depth change. The channel depth convergence rate γ_h is set to be zero ($L_h = \infty$), because there is no clear trend in channel depth in the mid-estuary region. The channel width has an overall landward decreasing trend, although local variations exist with expansions and convergences of O(100 m). Exponential fitting to the channel width yields an $L_w \approx 20$ km.

We can calculate the drag coefficient by rearranging Equation 11,

$$C_{D,energy} = \left(-\frac{\partial \left\| \eta \right\|}{\partial s} + 0.5(\gamma_w + \gamma_h) \left\| \eta \right\| \right) \frac{3\pi g \overline{H} \cos(\Delta\phi)}{4 \left\| U \right\|^2}. \tag{13}$$

The tidal energy flux balance (Equation 13) provides a method to calculate the drag coefficient different from Equation 3, as $C_{D,energy}$ represents the tidal energy loss due to drag. Tidal analysis was applied to the water level data collected by the three LT CTDs and the velocity U measured by the Aquadopp profiler at bend apex, with an analysis window length of 99 h (eight M2 tidal cycles). Tidal amplitude $\left\| \eta \right\|$ was calculated from the LT2 CTD data, $\left\| U \right\|$ was from the Aquadopp profiler collocated with the LT2 CTD, and $\Delta\phi$ is their phase difference. The tidal amplitude gradient was calculated between the LT1 and LT3 CTDs.

2.3.4. Bottom Friction Coefficient

The local near-bed shear stress was calculated from the high frequency ADV measurements near the bend apex. The bottom shear stress is quantified by the bottom friction coefficient C_f (similar to C_D, but only quantifies bottom stress), estimated using (e.g., Bowden & Fairbairn, 1956)

$$C_f = \frac{\overline{u'w'}}{\overline{u}^2} = \frac{\int S_{uw} \mathrm{d}k}{\overline{u}^2}. \tag{14}$$

$\overline{u}$ is the burst-averaged streamwise velocity. u' and w' are the temporal fluctuations of streamwise and vertical velocity around their means; $\overline{u'w'}$ is the Reynolds stress; S_{uw} is the wave number cospectrum of u' and w'.

Additionally, the C_f has been calculated from the near-bed dissipation rate ϵ (e.g., Kaimal et al., 1972) using law of the wall scaling

$$\epsilon = \frac{u_*^3}{\kappa z_a}, \tag{15}$$

where $u_* = \sqrt{\tau_b/\rho}$ is the shear velocity and τ_b is the bottom shear stress. $\kappa = 0.41$ is the von Kármán constant and $z_a = 0.5$ m is the height of ADV above the bed. Therefore,

$$C_f = \frac{u_*^2}{\overline{u}^2} = \frac{(\kappa z_a \epsilon)^{2/3}}{\overline{u}^2} \tag{16}$$

by substituting Equation 15. ϵ is estimated from the wave number spectrum of w'

$$S_{ww}(k) = a_0 \epsilon^{2/3} k^{-5/3} \tag{17}$$

with $a_0 = 0.68$ (e.g., Tennekes & Lumley, 1972).

3. Results

3.1. Estuarine Conditions

The laterally averaged water depth at the bend apex in the North River estuary ranges between 2 and 5.5 m as a result of tidal water level variation (Figure 2a), with the tidal range varying between 2 and 3.5 m from neap to spring tides. The water level is higher during flood tide than during ebb tide due to the phase difference between water level and velocity being less than 90° (examined below). The tides are dominated by the semi-diurnal M2 tide (1.2-m amplitude), with contributions from the S2 constituent (0.1 m), N2 constituent (0.3 m), and the diurnal K1 constituent (0.1 m). Stronger and weaker spring-neap tides appear each lunar month due to the N2 tidal constituent. During the observation period, the stronger spring tides occur around the end of each month. At the mooring locations, the tidal amplitude ranges between 0.9 and 1.5 m with increasing phase lag from LT1 to LT3 (Figure 3a). The tidal amplitude is similar between LT1 and LT2 and decreases at LT3. Note that the analysis used a 99-h low-pass filter window, so the calculated tidal amplitude may be slightly different from the range of fluctuations in the original water depth record. The tidal velocity amplitude varies between 0.35 and 0.55 m/s and the velocity phase leads that of the water level by 45 (spring tides) to 55 (neap tides) degrees, so the tidal wave is partially progressive (Figure 3b).

Stratification is calculated as the surface-to-bottom salinity difference ΔS (Figure 2c). Stratification is stronger early in the observation period (before mid-June) due to the greater freshwater discharge. The greatest

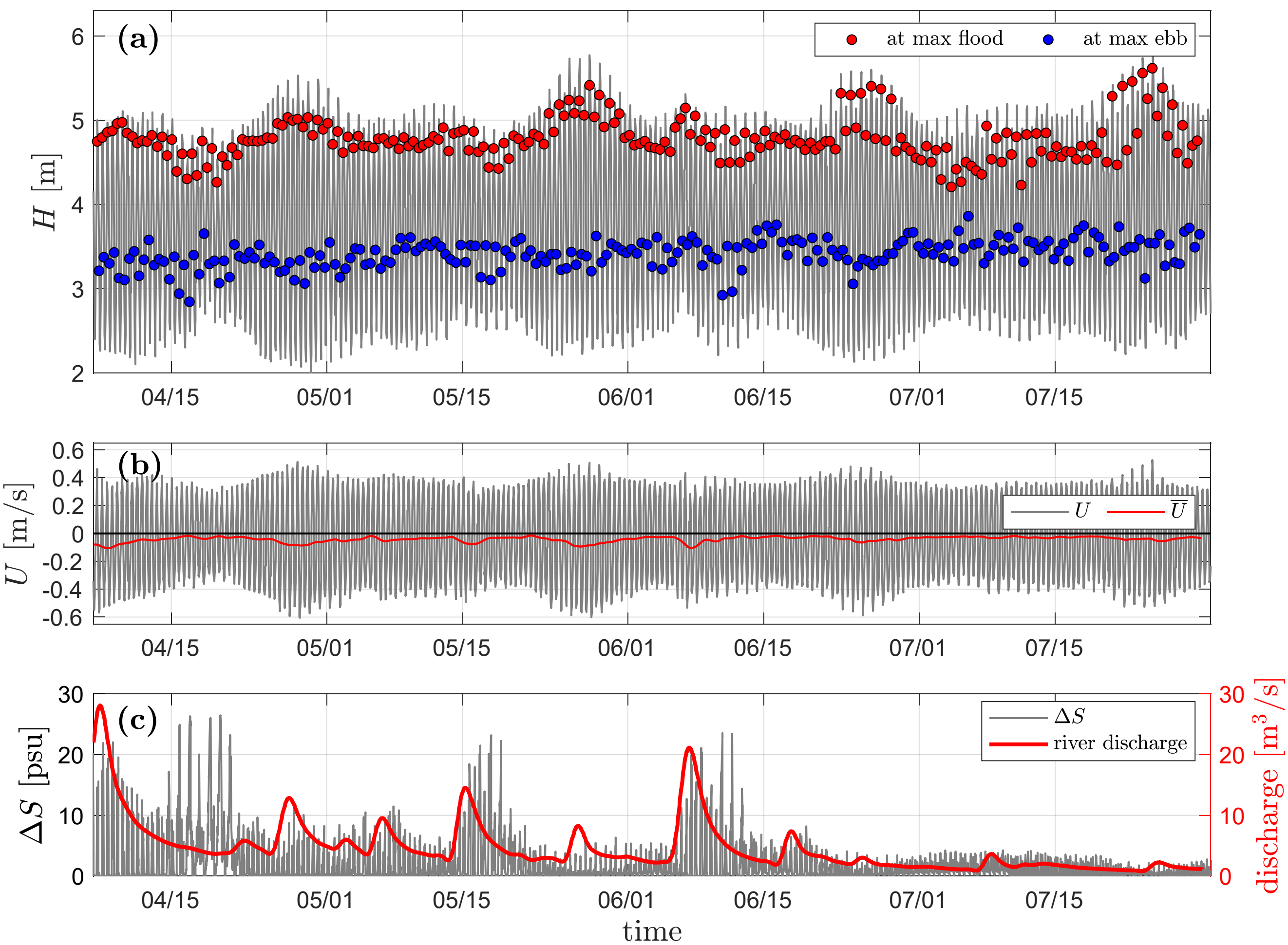

Figure 2. (a): Water depth at the bend apex in the North River estuary. Red dots represent water depth at max flood tide; blue dots at max ebb tide. (b): Black line: depth-averaged velocity at the bend apex; red line: low-pass filtered (33 h) velocity. $U > 0$ is flood tide. (c): Left axis: stratification (surface-to-bottom salinity difference) at the bend apex; right axis: river discharge.

stratification (e.g., $\Delta S > 10$ psu) is found during high discharge events or neap tides. Tidally, stratification is most common from max flood tide through late flood and early ebb tide, and ΔS is less than 1 psu at max ebb tide except for during the weakest neap tides (less than 10% of the data record). Stratification is weaker in the summer (after mid-June) when freshwater discharge is less, with peaks of $\Delta S \sim 1 - 5$ psu during early flood and ebb tides and $\Delta S < 1$ psu mostly during the rest of the tidal cycle. Therefore, we describe the North River estuary as intermittently stratified.

The time-mean BTPG on the North River estuary was estimated using the mean momentum balance (Equation 9) by calculating the tidal stress, the mean flow bottom friction, and the mean BCPG (Figure 3c). The mean flow friction increases during high discharge periods or high spring tides when a stronger mean current is generated due to greater Stokes drift (e.g., Uncles & Jordan, 1980); the tidal stress increases during high spring tides because tidal decay is more rapid when tidal forcing is stronger (Appendix A); the mean BCPG decreases during high spring tides because of the greater salinity intrusion length. The three terms have similar magnitudes, but the tidal stress is more sensitive to tidal forcing and can be dominant during high spring tides. The time-mean BTPG calculated from these three terms is large during large spring tides (e.g., in late April, May, June, and July) and during several high discharge events (e.g., in early April and early June). The seaward mean flow results in a landward bottom friction. The tidal stress is in the direction of decreasing tidal amplitude, so it is mostly landward in this shallow and weakly converging estuary, except in early July when the tidal stress becomes seaward because the tidal amplitude is larger at mooring site LT3

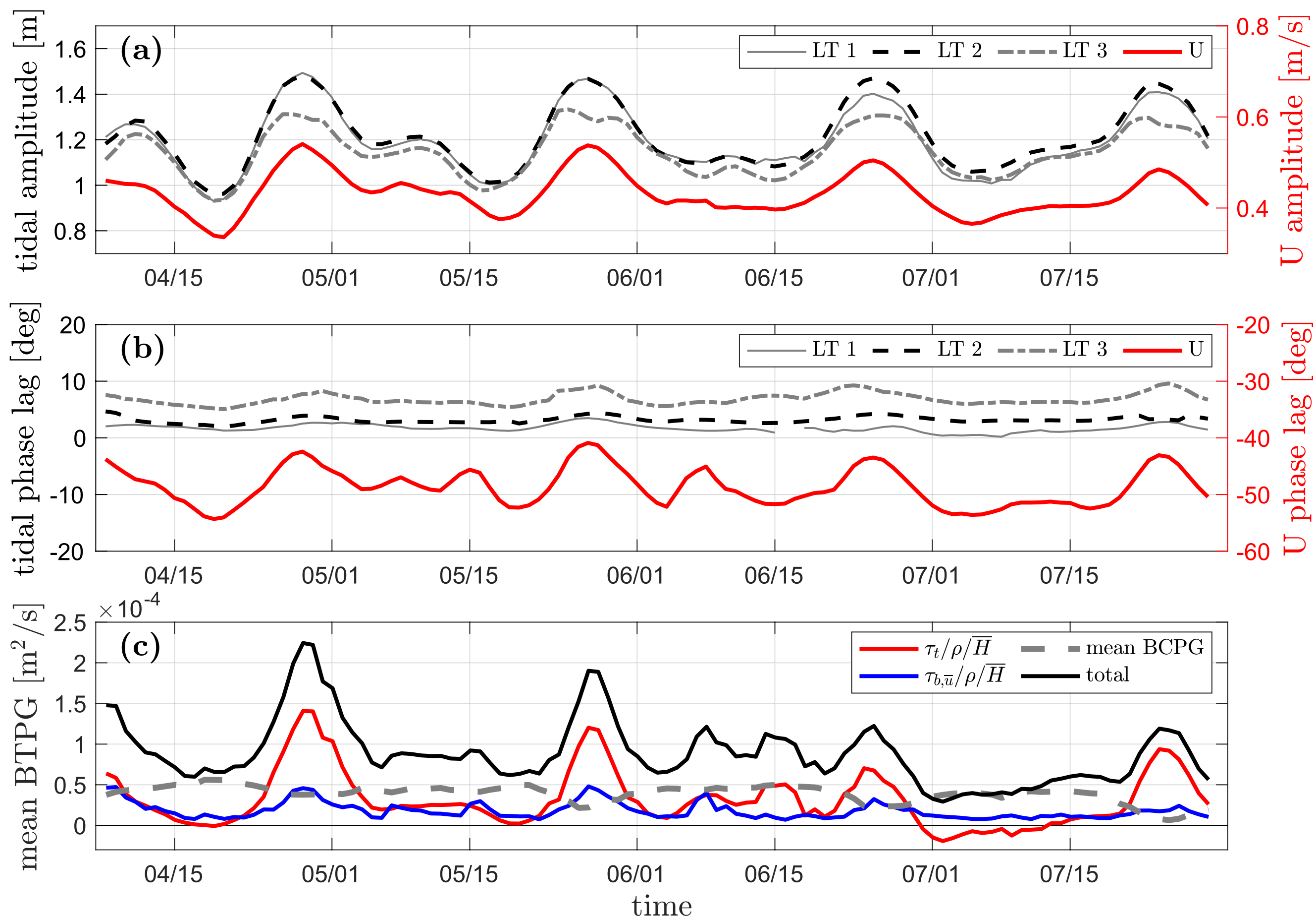

Figure 3. (a): Left axis: tidal amplitude at LT1, LT2, and LT3; right axis: velocity amplitude at LT2. (b): Left axis: tidal phase lag at LT1, LT2, and LT3, referenced to the tidal phase near the estuary mouth; right axis: velocity phase lag at LT2. Note the difference in vertical axis range. (c): Terms that contribute to the mean along-channel barotropic pressure gradient (BTPG). The red line represents the tidal stress; the blue line represents the mean bottom friction; the dashed gray line represents the mean baroclinic pressure gradient (BCPG); and the black line is the total of the above three terms that is balanced by the mean BTPG.

than LT1 (Figure 3a). The mean BCPG has a landward forcing because salinity decreases from seaward to landward. The mean BTPG balances these three terms, and always provides a seaward forcing during the observational period (Figure 3c), that is, a water level setup at the landward side.

3.2. Drag

The drag coefficient C_D is calculated using Equation 3 (Figure 4a) and it represents the total momentum loss between mooring sites LT1 and LT3. The total BTPG is the dominant term that balances the drag in the momentum budget, similar to other studies in the coastal regions (e.g., Lentz et al., 2017; Monismith et al., 2019; Rogers et al., 2018). The BCPG is about an order of magnitude smaller than the BTPG in most of the observational period, except during neap tides and high discharge events when the BCPG can be up to 30% of the BTPG for ebb tides and 50% for flood tides. The C_D values calculated from the mooring observations are generally in the range of $5 \times 10^{-3} - 20 \times 10^{-3}$ (Figure 4a). C_D values during both flood and ebb tides are higher than the typical values of ~3×10^{-3} and show large temporal variability. Averaging over the observation period, C_D is greater during flood tide (12×10^{-3}) than ebb tide (10×10^{-3}) (Figure 4c). The highest calculated values (up to 25×10^{-3}) correspond to flood tides, and flood tide C_D values are notably greater than ebb values during high spring tides, for example, late April, late May, and late July. Application of the two-sample -test to the flood C_D and ebb C_D indicates that they have unequal means and the flood-ebb asymmetry is significant.

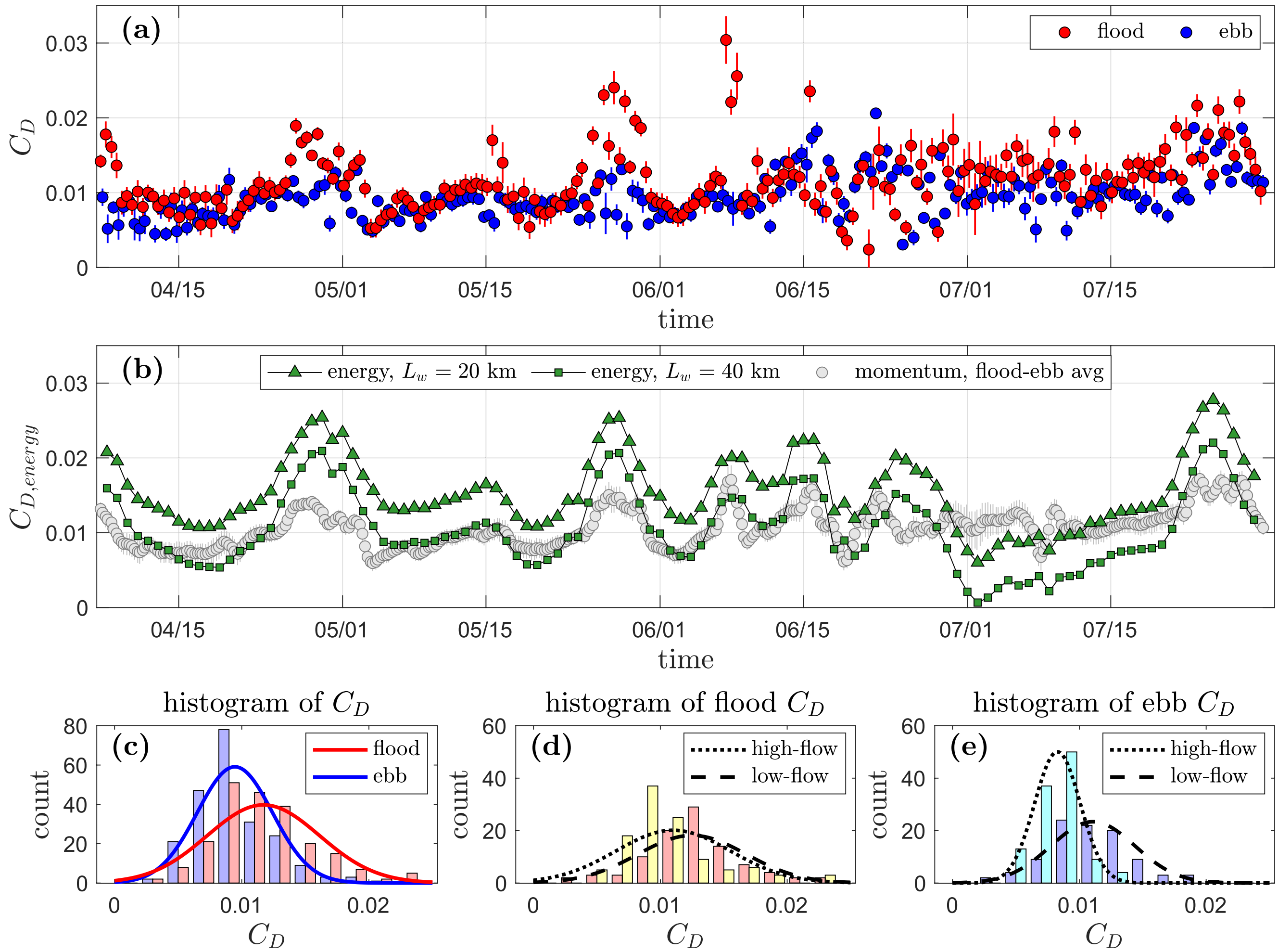

Figure 4. (a): Drag coefficient C_D in the North River estuary calculated from the momentum balance. Red dots represent C_D at max flood tide and blue dots at max ebb tide. Vertical lines show the larger of the instrument error and the standard deviation within each 1-h window around max flood and ebb tide. (b): Drag coefficient $C_{D,energy}$ calculated by energy flux balance. Green triangles are based on a width convergence distance L_w = 20 km; green squares use L_w = 40 km; and gray circles are the flood-ebb averaged C_D from momentum balance in (a). (c): Histograms of flood tide C_D and ebb tide C_D. (d): Histograms of high-flow season flood C_D (before mid-June) and low-flow season flood C_D (after mid-June). (e): Histograms of high-flow season ebb C_D and low-flow season ebb C_D. Lines show the Gaussian curve fits.

A seasonal difference can also be observed in the ebb tide C_D (Figure 4e). Most high values of C_D during the ebb tide (e.g., >10×10^{-3}) are found in the low-flow season (starting from mid-June), resulting in a higher average C_D in the low-flow season (11×10^{-3}) than in the high-flow season (8×10^{-3}). In contrast, flood tide C_D has a less clear seasonal difference (Figure 4d), with average values of 12.5×10^{-3} in the low-flow season and 11×10^{-3} during high flow.

It is worthwhile to note that the calculation of C_D includes the estimation of the time-mean BTPG (Section 3.1). The seaward mean BTPG opposes the tidal BTPG during floods, and it is additive to the tidal BTPG during ebbs. The mean BTPG on average corresponds with an adjustment of C_D of $2 - 3 \times 10^{-3}$ (20–30% of the total C_D) and including the mean BTPG reduces the tidal asymmetry in the calculated C_D.

$C_{D,energy}$ is calculated from the energy flux balance using Equation 13 (Figure 4b) and it reflects the tidal energy dissipation. Generally, $C_{D,energy}$ is $5 \times 10^{-3} - 20 \times 10^{-3}$ with the largest values during high spring tides, in agreement with the C_D from the momentum balance. $C_{D,energy}$ calculated using L_w = 20 km, as suggested by the exponential fitting (Section 2), is generally greater than the tidally averaged C_D from the momentum budget. Using L_w = 40 km instead results in $C_{D,energy}$ values that are more consistent with the momentum calculation. $C_{D,energy}$ has particularly low values around July 1 when the tidal amplitude increases from LT1 to LT3 (Figure 3a). The overall high values of $C_{D,energy}$ indicate a high rate of tidal energy dissipation that is broadly consistent with the high C_D calculated from the momentum balance. Moreover, the calculation of $C_{D,energy}$ is independent of estimation of the mean BTPG, since it is based on the tidal amplitude decay rate instead of the instantaneous water level gradient. The values of $C_{D,energy}$ that are comparable with momentum-balance estimates of C_D provide corroborating evidence for the high values of effective drag coefficient.

In the following analysis, we used the C_D from the momentum balance, since it can be assessed for each flood and ebb tide and because it does not require the estimation of the channel convergence rate.

3.3. Uncertainty of the Calculated Drag Coefficient

The uncertainty in the C_D calculated from the momentum balance is contributed by two categories of factors: instrument error and estimation of the momentum budget. Based on the accuracy of the pressure sensors and velocity measurements, we estimate that the instrument error leads to a relative uncertainty in C_D of less than 10%. The approximation of the momentum budget from observed quantities also introduces uncertainty in the calculated C_D, because estimation based on single-location measurements cannot fully represent the cross-channel and along-channel variability of the North River estuary, and because we have made simplifications to the momentum equation, for example, neglecting the advection term and estimating the time-mean pressure gradient. The drag term is greatest and most insensitive to errors induced by different sources of uncertainty around maximum flood and ebb tide, so the reported values of C_D are for 1-h windows around max tides.

The velocity data were collected by the LT2 Aquadopp near the outer bank, but the depth-averaged velocity can also have lateral variability. Therefore, the Aquadopp data were compared with the cross-sectional average velocity from ADCP surveys near the mooring. Based on the comparison of 10 tides, the Aquadopp measurements were nearly the same as the cross-channel average, with less than 5% deviation. Therefore, using the depth-averaged velocity from the mooring is not likely to cause significant bias or uncertainty in C_D. Cross-channel bathymetry is not uniform at the bend apex, and we have used the laterally averaged depth H as being more representative than the single depth at the velocity measurement location.

The LT2 mooring site was near the bend apex, and the lateral structure of the depth and velocity also varies along the channel. To estimate the influence of the along-channel geometry on C_D, we integrated the momentum balance along the channel between LT1 and LT3 following a method as in Lentz et al. (2017). This approach uses bathymetric data, assumes mass flux conservation to estimate the velocity variability, and simplifies the momentum balance to a balance between the water level gradient and drag. Based on this along-channel integration, we estimate that along-channel variability in channel geometry may reduce the C_D calculated at the bend apex by up to 10% for flood tide and up to 30% for ebb tide. This is due to the width convergence and depth decrease landward of the bend, which in the along-channel integration corresponds with increased velocity and a reduction in C_D. Ebb tide C_D is more sensitive to along-channel depth variations than flood tide, because water is shallower during ebbs. The along-channel variability of bathymetry may contribute to larger values of C_D calculated at the bend, but it is not a sufficient explanation, particularly for flood tides when the highest drag was observed. Furthermore, the channel geometry factors alone suggest that ebb tide C_D would be larger than flood tide C_D, but the opposite flood-ebb asymmetry was observed. Incorporating more accurate estimates of the along-channel variability in the momentum budget could lead to lower values of C_D and enhance the observed flood-ebb asymmetry, but that would require much better spatial resolution of velocity and water level.

The advection and Coriolis terms were neglected when simplifying the momentum equation, and the resulting uncertainty is estimated to be small. The estimated time-mean pressure gradient is an order of magnitude smaller than the directly measured tidal pressure gradient, so the uncertainty in the estimation of time-mean pressure gradient represents a higher-order error for the tidal momentum balance and calculation of C_D, and is thus negligible.

The standard deviation of C_D was reported for each 1-h window around max flood and ebb tides to show the potential uncertainty caused by the estimation of the momentum budget. The standard deviation of C_D is generally less than 10% of the drag value except from late June to early July (Figure 4a) when it can be in the range of 10% to 40%. Note that the along-channel variability may introduce a bias that is not totally

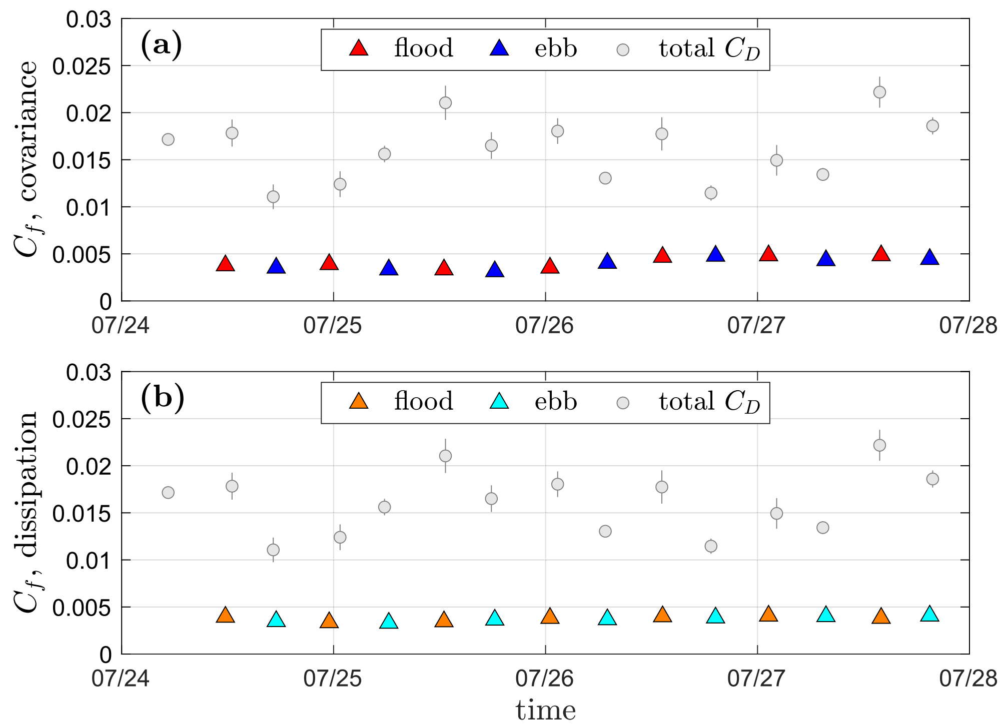

Figure 5. Acoustic Doppler velocimeter (ADV) measurement from July 24 to July 27. (a): Bottom friction coefficient C_f calculated from the covariance method (Equation 14), (triangles, averaged over multiple ADV bursts in flood or ebb tides). Gray circles show the total C_D from momentum balance in Figure 4a as a comparison. (b): Bottom friction coefficient C_f calculated from the dissipation method (Equation 16).

accounted for by the reported standard deviations, so C_D could be up to 10%–30% lower than the plotted error bars, especially for ebb tides. Overall, the uncertainty estimates are modest compared to the magnitude and temporal variability of C_D in the observations, and the drag estimates from the momentum balance are considered to be robust based on the uncertainty analysis.

3.4. Local Bottom Shear Stress

The bottom friction coefficient C_f was estimated using both Equation 14 and Equation 16. The tidal-phase averaged values of C_f from the ADV measurements are consistent between the two methods and range between 3×10^{-3} and 5×10^{-3} (Figure 5), which is similar to values for C_D due to bottom roughness in other estuaries (e.g., Heathershaw & Simpson, 1978; Seim et al., 2002). However, C_D calculated from the momentum balance during the same time period ranges between 11×10^{-3} and 18×10^{-3} for ebb tides and $13 \times 10^{-3} - 22 \times 10^{-3}$ for flood tides. The total drag C_D is larger than the bottom stress C_f by a factor of 3–5, indicating the existence of other sources of drag in addition to bottom friction. Form drag due to flow separation at sharp channel bends could contribute to this high total drag as well as other potential factors, including secondary circulation in bends, form drag from bedforms in the channel, and friction from flow through marsh vegetation.

3.5. Dependence on Water Depth and Discharge

Tides and river discharge provide the dominant forcing in this estuary, and we investigate the dependence of C_D on these two factors. Tidal conditions could affect the drag through creating variation in water level, velocity amplitude, and flow structure. The calculated C_D does have a slightly increasing trend with water depth, with $R^2 = 0.1$ and $\text{p-value} < 0.001$ (Figure 6a). C_D does not correlate with the tidal velocity ($R^2 = 0.0$, $\text{p-value} > 0.05$, not shown). The depth dependence primarily reflects the flood-ebb asymmetry in C_D noted previously. Water levels are higher during flood tides than ebb tides (Figure 2a), and flood tide

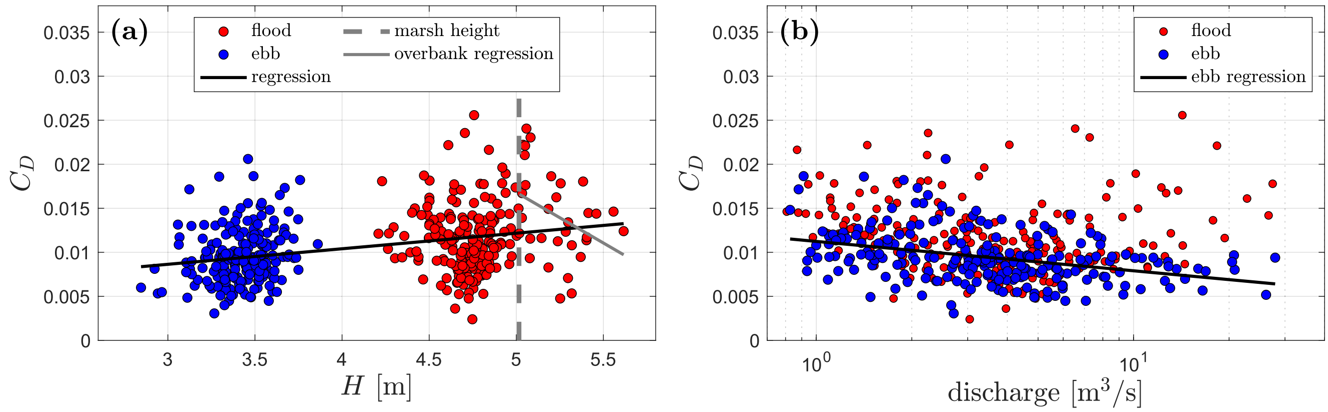

Figure 6. (a): Drag coefficient versus water depth at the bend apex. Linear regressions give $R^2 = 0.10$ (p - value < 0.001) for the overall data and $R^2 = 0.14$ (p - value $= 0.03$) for the overbank cases (water depth exceeds marsh height). (b): Drag coefficient versus river discharge. $R^2 = 0.13$ (p - value < 0.001) for ebb tides, and $R^2 = 0.00$ (p - value > 0.05) for flood tides.

C_D has a greater average value than ebb tide C_D. The flood-ebb asymmetry in C_D is most apparent during high spring tides (Figure 4a) when the flood-ebb difference in water level is also greatest (Figure 2a). In addition, zooming in on the cases with overbank flow, C_D shows a decreasing trend with water depth for overbank flow conditions, opposite to the overall increasing trend. Possible reasons for the observed depth dependence of C_D will be investigated in the following analysis.

River discharge creates a seaward mean flow that influences the salt balance in addition to momentum, and thus affects the salinity intrusion, along-estuary salinity gradient, and stratification (Geyer, 2010). The salinity field affects the momentum budget through the along-estuary BCPG, and stratification can also reduce drag by damping turbulence. In the observations, the ebb tide C_D has a negative correlation with river discharge (Figure 6b). This negative correlation is reflected in the seasonal trend in the ebb tide C_D, where lower ebb C_D values occur during the higher discharge season and ebb C_D values increase in summer as river discharge decreases (Figure 4e). In contrast, the flood tide C_D shows no significant dependence on river discharge, and this corresponds with the less apparent seasonal variation in flood C_D values (Figure 4d). Factors that may be contributing to the observed discharge dependence will also be addressed in the analysis.

4. Analysis

4.1. Flow Separation and Adverse Pressure Gradient

The high C_D in the North River estuary suggests the existence of other sources of drag beyond bottom friction, and one source could be flow separation in the lee of bends (e.g., Leeder & Bridges, 1975; Leopold, 1960). An idealized modeling study by Bo and Ralston (2020) found that flow separation in sinuous estuarine channels results in significant form drag. In a sinuous channel with geometric parameters similar to the North River (e.g., bend sharpness and aspect ratio), the total C_D increased to around 12×10^{-3} due to flow separation and the resulting form drag. In the model results, C_D also increased with water depth in a manner consistent with the tidal differences in water level and C_D observed in the North River (Section 3.5). The positive depth-dependence in the model study was because the flow separation and form drag became stronger in deeper water (Bo & Ralston, 2020).

In the cross-channel ADCP surveys in the North River, flow separation was observed in the velocity field downstream of the sharp bend (Figure 7). Depending on the tide, flow near the inner bank was decelerated relative to the main current, and in some cases, flow reversal was observed in the lee of the bend. Similar patterns of flow separation and reversal were also found in field, laboratory, and modeling studies of curved channels, for example, Ferguson et al. (2003), Finotello et al. (2020), Blanckaert (2015), and Bo and Ralston (2020). In many river bends, point bars form at the inner bank, and the shallower bathymetry there leads to topographic steering and contributes to the deceleration of flow at the inner bank (e.g.,

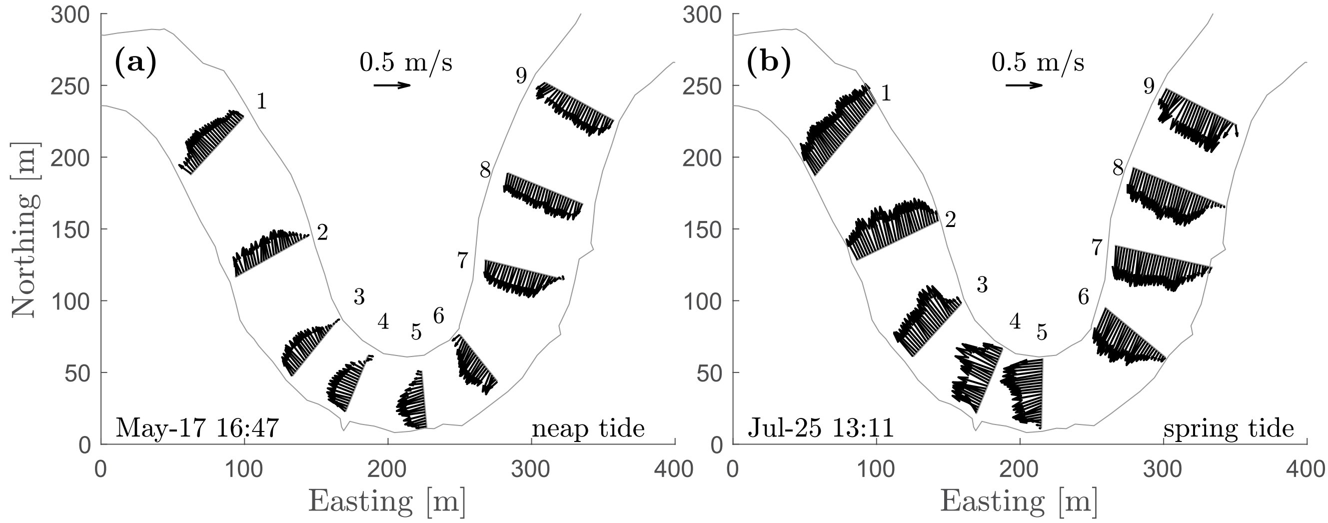

Figure 7. Depth-averaged velocity field during flood tides. (a): Neap flood tide in mid-May. (b): Spring flood tide in early July.

Dietrich & Smith, 1983). In the North River bend, the cross-channel bathymetry is relatively symmetric (Section 2.1), so the deceleration and flow reversal near the inner bank is not primarily due to topographic steering (Kranenburg et al., 2019). Instead the curvature effect on the pressure field is likely the predominant mechanism for generating the observed flow separation.

The channel curvature results in a cross-channel water level slope at the apex of this bend (Kranenburg et al., 2019), while the lateral differences in water level upstream and downstream of the bend are nearly zero. As a result, the water level at the inner apex is lower than the downstream exit of the bend, and an adverse pressure gradient occurs along the inner bank downstream of the apex. This adverse pressure gradient can lead to convex bank flow separation and produce a low pressure "separation zone" in the lee of bends that thus creates the form drag (e.g., Blanckaert, 2010; Blanckaert et al., 2013; Bo & Ralston, 2020; Ferguson et al., 2003).

We examine the pressure gradient downstream of the bend apex to assess the potential for flow separation and form drag. We have focused on the flood tide in the adverse pressure gradient analysis because the short-term (ST) instrument array better resolved the local pressure gradient during the flood (Section 2.2). The water level difference ($\Delta\eta$) between the CTD downstream of the bend (ST3A) and the CTD at the apex near the inner bank (ST2C) was calculated to estimate the along-inner-bank pressure difference (Figure 8). In doing so, we have assumed that the water level is laterally uniform at the downstream exit, and the ST3A measurement at the outer bank can represent the inner bank water level. This assumption is reasonable because channel curvature is weak there (Figure 8a), and Kranenburg et al. (2019) reported negligible lateral water level differences at the exit of this bend. Note that we have focused on the barotropic pressure, that is, the water level, because the baroclinic pressure gradient is usually much smaller. The measured $\Delta\eta$ is on the order of centimeters, comparable to the instrument accuracy and the high-frequency water surface variability due to capillary waves and boat wakes. Thus, the data have been averaged over 2-min intervals (360 samples) to reduce random noise and instrument error and increase measurement precision.

The water level difference $\Delta\eta$ is positive during ebb tide (Figure 8), consistent with the downstream favoring pressure gradient that drives the seaward current. Entering flood tide, the flow direction turns and $\Delta\eta$ becomes negative, consistent with a favoring pressure gradient. However, as the landward tidal current keeps growing, the adverse pressure gradient associated with the curvature effect occurs and this can be seen in the upward peaks in $\Delta\eta$ during flood tides in Figure 8. This positive, or adverse, $\Delta\eta$ around max flood tide creates the adverse pressure gradient downstream of the bend along the inner bank that corresponds with flow separation.

To assess the potential influence of flow separation and form drag on the observed C_D, we examine the correlation between the drag and adverse pressure gradient along the inner bank. The adverse pressure

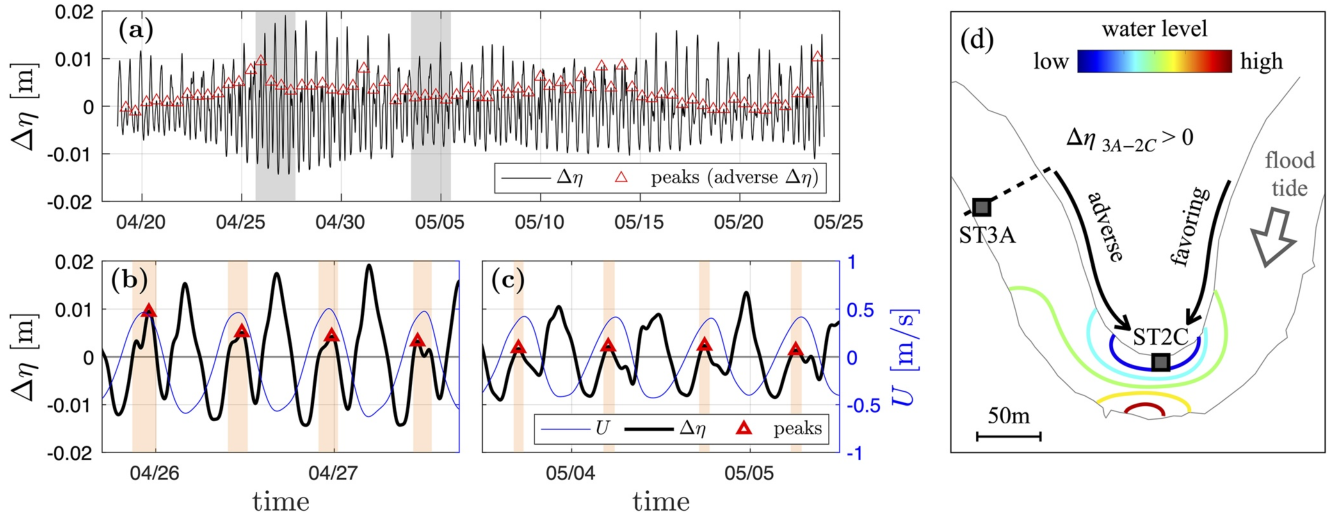

Figure 8. (a): Water level difference ($\Delta\eta$) between conductivity-temperature-depths (CTDs) ST3A and ST2C. Red triangles mark the peaks of adverse η_s. The gray bands represent the zoomed-in time periods shown in panels (b) and (c). (b), (c): $\Delta\eta$ and adverse $\Delta\eta$ in late April (spring tide) and early May (neap tide). The left vertical axis shows $\Delta\eta$ (black line) and the right vertical axis shows U (blue line), the depth-averaged velocity at the apex. Orange bands mark the periods when adverse pressure gradient appears. $U > 0$ is flood tide. (d): A schematic of the adverse pressure gradient in the bend, with contours of the water level field.

gradient was calculated using the short-term measurements (in April and May), so only the corresponding part of the C_D record (calculated using the long-term moorings) is examined. The C_D calculated from the large-scale LT measurements is significantly correlated with the bend-scale adverse $\Delta\eta$ from ST measurements ($R^2 = 0.25$ and p - value < 0.001), with C_D increasing as the adverse pressure gradient increases (Figure 9). While the spatial and temporal coverage of the observational data is limited, the trends in the available evidence are consistent with the explanation that flow separation, as reflected in the strength of the adverse pressure gradient measured at the sharp bend of the study, contributes to the high drag found in the North River estuary.

The adverse pressure gradient for ebb tide is not investigated due to the lack of pressure measurement at the down-estuary exit of the bend. Flow separation was also observed in the ebb tide velocity field with decelerated flow near the inner bank (not shown), although the velocity field during ebb is also affected by topographic steering associated with the relatively shallow shoal near the inner bank at the down-estuary side of the bend (Figure 1). According to the previous idealized modeling results, flow separation is expected to be weaker during ebb tide because of the shallower water depth and greater influence of friction (Bo & Ralston, 2020).

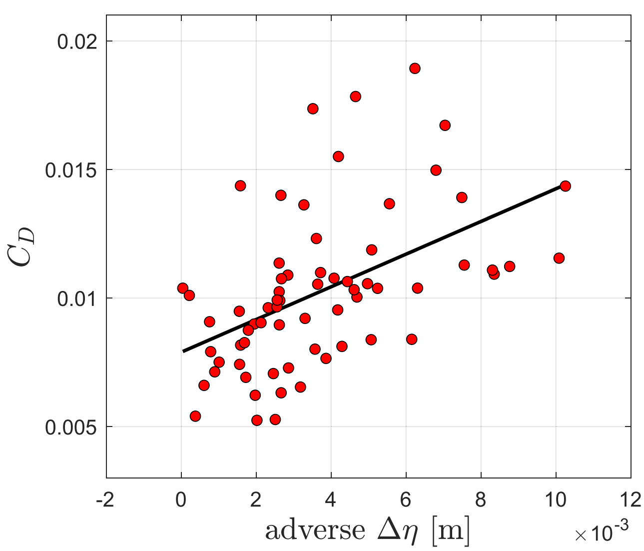

Figure 9. Correlation between the drag coefficient and adverse $\Delta\eta$ that appears at flood tide. $R^2 = 0.25$ (p - value < 0.001).

4.2. Overbank Flow

During high spring tides, the water level exceeds channel bank height and marshes are inundated. The marsh height at the bend apex corresponds to a water depth of ~5 m. The high spring tides in late May and late July are plotted in Figure 10 as an example. Water level displays a diurnal variation due to the K1 tidal component and channel flow substantially goes onto the marsh at the higher flood tide, every other tidal cycle.

The drag coefficient also shows a diurnal variation, with C_D that is smaller during the flood tides that have overbank flow compared to the prior and subsequent tides. The marsh platform is vegetated, and the overbank flow through the marsh vegetation might be expected to increase the total drag due to stem friction. Instead, the total drag is decreased with

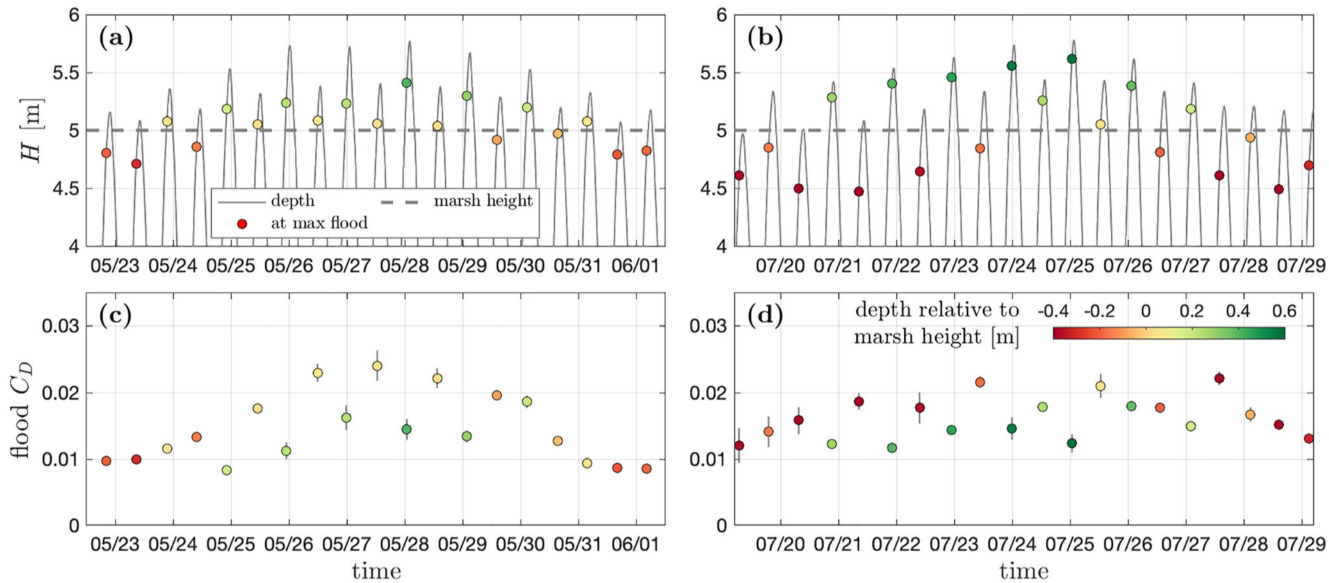

Figure 10. Water depth H and flood-tide drag coefficient C_D during high spring tides in late May and late July. (a): Water depth in late May; (b): water depth in late July; (c): flood tide C_D in late May; and (d): flood tide C_D in late July.

overbank flow. The reduced values of C_D during flood tides with overbank flow is also counter to the overall relationship of drag increasing with water depth (Figure 6a) and is opposite to the depth dependence expected from flow separation (Bo & Ralston, 2020).

A potential explanation for the decrease in C_D with overbank flow could relate to the inhibition of flow separation. While deeper water facilitates flow separation, increased bottom friction due to the shallow overbank flow and stem friction from flow through vegetation could inhibit flow separation. The frictional effect is illustrated by dimensionless numbers from theoretical models that predict flow separation, for example, $H/(C_f W)$ in Blanckaert (2010), where H is water depth, C_f is the friction coefficient, and W is channel width, and $H/(C_f L)$ in Bo and Ralston (2020) with L being the bend length. The underlying mechanism of these theoretical models is that stronger bottom friction diminishes the local adverse pressure gradient along the inner bank and inhibits flow separation. The effective C_f increases for overbank flow because of both the shallower water depth over the marsh and the stem friction of vegetation. As a result, flow separation that creates form drag is inhibited when flow goes onto the marsh and the total drag is decreased, even though locally flow over the marsh has relatively large friction. The overbank flow effect is reflected in the depth dependence plot, where C_D shows a decreasing trend when water depth exceeds the marsh platform height (Figure 6a). Similar results were reported for laboratory experiments by Marriott (1998) where flow separation occurred in a sinuous channel but did not occur when flow was overbank. Similarly, James et al. (2001) found that vegetation can inhibit flow separation in sinuous laboratory channels and decrease the total drag, consistent with the decreased C_D for flow over the marsh in the North River estuary.

4.3. Stratification and Baroclinic Effects

The dependence of C_D on river discharge (Figure 6b) suggests that baroclinic effects may play a role in flow separation and the drag. In this subsection, we describe an observed interaction between stratification and secondary circulation during ebb tides, and propose a baroclinic mechanism that can potentially reduce the adverse pressure gradient along the inner bank, and thereby inhibit flow separation and decrease the drag.

During ebb tides, a normal secondary circulation is observed in the cross-section at the apex (Figure 11). When the channel is stratified, this normal secondary circulation brings high salinity water to the inner bank and tilts the isohalines up near the bend apex. Downstream of the bend, the lateral circulation is weaker and has less effect on the lateral salinity distribution, so the isohalines are relatively flat. Similar isohaline

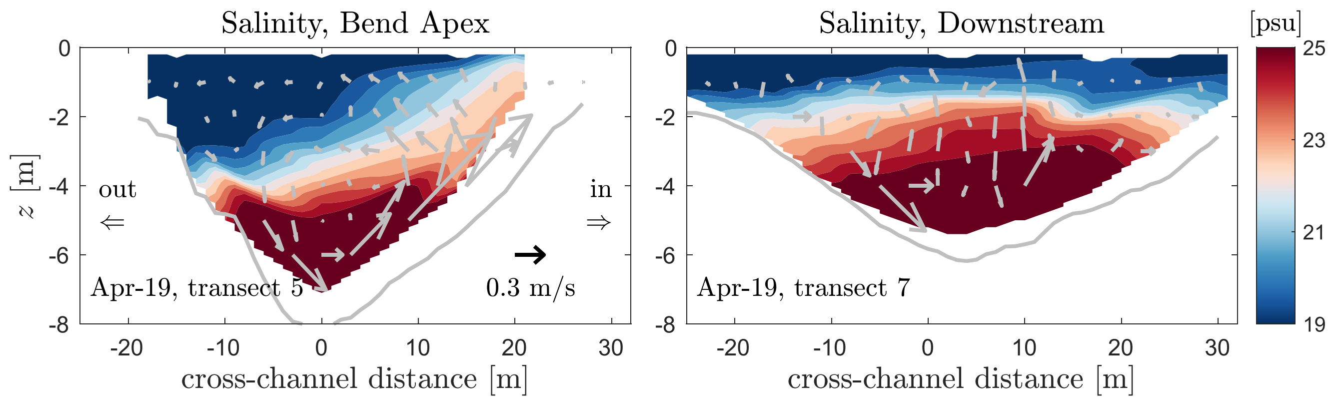

Figure 11. Salinity and secondary circulation in two cross-sections at the apex (transect 5) and downstream (transect 7) during an early ebb tide with strong stratification.

tilting has been observed in, for example, Seim and Gregg (1997) and Chant (2002). The lateral circulation resulting from flow curvature creates a bulge of high salinity water near the inner bank at the bend apex. During the ebb, this high salinity at the inner bank of the apex exerts a favoring baroclinic pressure gradient downstream of the apex that counteracts the adverse barotropic pressure gradient downstream of the bend created by the flow curvature (Section 4.1). Consequently, the interaction between the lateral circulation and stratification could inhibit flow separation and reduce the form drag around bends.

The next question is whether the favoring baroclinic pressure gradient along the inner bank due to the lateral circulation is large enough to balance the barotropic adverse pressure gradient created by the curved streamwise flow. The baroclinic pressure gradient can be directly calculated using $\beta g(\partial S_{in}/\partial s)H_{in}$, where S_{in} and H_{in} are the depth-averaged salinity and depth at the inner bank. The barotropic pressure gradient is estimated from the along-inner-bank momentum balance

$$g\frac{\partial \eta_{in}}{\partial s} = -U_{in}\frac{\partial U_{in}}{\partial s} - C_f\frac{U_{in}\,|U_{in}|}{H_{in}} = adv. + frict., \tag{18}$$

where U_{in} is the depth-averaged velocity at the inner bank. On the right side of Equation 18 are the advection and friction terms that determine adverse pressure gradient and flow separation in homogeneous fluids (Bo & Ralston, 2020). The barotropic and baroclinic pressure gradients are estimated using the cross-channel surveys during an early ebb tide on April 19 (transects 5 and 7, Figure 7). U_{in} and H_{in} are calculated from the cross-channel ADCP measurements and S_{in} is from the shipboard CTD measurements, each taken as the average over 10 m from the inner bank (S_{in} = 22.6 psu at transect 5 and S_{in} = 20.9 psu at transect 7, Figure 11). The advection term contributes to an adverse pressure gradient and the friction term contributes to a favoring pressure gradient, which is consistent with theoretical models that predict flow separation in Signell and Geyer (1991) and Bo and Ralston (2020). The barotropic pressure gradient that is the sum of the advection and friction terms is positive (~1–6 × 10^{-4} m/s^2), indicating an adverse pressure gradient that can cause flow separation downstream of the apex. In contrast, the baroclinic pressure gradient is negative (∼− 2 × 10^{-4} m/s^2) and can counteract the adverse pressure gradient. Downstream of the apex, the favoring baroclinic pressure gradient is of the same order of magnitude as the adverse barotropic pressure gradient, suggesting that the salinity effect has the potential to inhibit flow separation.

This baroclinic inhibition of flow separation may explain the variation in ebb tide C_D with the river discharge (Figure 6b). The along-inner-bank baroclinic pressure gradient results from the interaction between the stratification and secondary circulation during the ebb tide. Stratification is stronger in the high-flow season, which can lead to stronger baroclinic pressure gradients and weaker flow separation, and thus reduce ebb tide C_D. Under low-flow conditions, stratification is weak, and while the lateral circulation is still present, the baroclinic pressure gradient due to tilting of isopycnals disappears.

The direct effects of stratification on damping turbulence and reducing the bottom friction could be another reason for the observed negative correlation between ebb tide C_D and discharge. Stratification becomes stronger during higher discharge periods and it can inhibit turbulence (Geyer, 1993), alter vertical momentum distribution, and decrease the bottom shear stress. However, the bottom stress is not the dominant contributor to the total C_D (Section 3.4), and the inhibition of bottom friction alone is insufficient to explain the discharge dependence of C_D. The variation in ebb tide C_D with river discharge is more than 5×10^{-3} (Figure 6b), which is greater than the local estimates of C_f (Figure 5).

The ebb tide C_D is negatively correlated with ΔS, but the correlation only holds for ΔS during the early ebb ($R^2 = 0.2$ and p - value < 0.001) not for ΔS at max ebb tide ($R^2 = 0.0$ and p - value > 0.05) because stratification has typically mixed away by max ebb. C_D is calculated from the momentum balance around max ebb tide (Section 2.3.1), suggesting that the inhibition of flow separation by stratification has a lagged effect. Stratification can impede the growth of adverse pressure gradient during early ebb tide so that flow separation is not fully developed at max ebb, even if stratification has disappeared at that time. In contrast, the inhibition of bottom shear stress by stratification happens instantaneously. Any inhibition of turbulence and bottom shear stress by stratification during early ebb is unlikely to affect bottom shear stress at max ebb, which further indicates that the discharge dependence of C_D is not due to the direct inhibition of turbulence by stratification.

The secondary circulation is more complex during flood tide, as the sense of secondary circulation can be reversed and multiple circulation cells are formed (Kranenburg et al., 2019). The interaction between stratification and the secondary circulation during flood tide, as well as any influence on flow separation and drag are still unknown.

4.4. Bed Roughness

The bottom friction appears to contribute less than form drag to the increased total drag, given that the bottom friction coefficient C_f is around $3 \times 10^{-3} - 5 \times 10^{-3}$, much smaller than the total drag coefficient C_D (Sections 3.2 and 3.4). The C_f calculation was based on the ADV measurements near the apex of bend, and the calculated C_f values correspond with a log-layer estimate for the bottom roughness of $z_0 = 0.002{-}0.005$ m (e.g., Lentz et al., 2017). However, the bathymetry survey of the North River (Section 2.2) indicates that the bedforms vary in size along the estuary and that in some areas, the bed roughness elements may be much larger than this local estimate from the ADV would suggest.

We estimate the bottom roughness scales quantitatively by using the detrended bathymetry data following an approach as in Rogers et al. (2018). Mega ripples are found at several locations near the sharp bend with roughness height h_b of 0.1–0.5 m and wavelength λ_b of 1–10 m, and bedform crests are generally oriented perpendicular to the along-channel flow. The bedform steepness h_b/λ_b is generally in the range of 0.05–0.1. The bottom roughness z_0 due to these bedforms is estimated as

$$z_0 = a_1 h_b \frac{h_b}{\lambda_b}, \tag{19}$$

where a_1 is a linear roughness coefficient (e.g., Grant & Madsen, 1982; Rogers et al., 2018). a_1 is typically in the range of 0.3–3 (Soulsby, 1997; Trowbridge & Lentz, 2018) and here, we assume $a_1 = 1$ as an estimate. Based on this, the mega ripples in the North River correspond to a z_0 of 0.002–0.05 m and a depth-averaged drag coefficient of up to 0.01 (Lentz et al., 2017). These higher values of z_0 apply only in parts of the estuary rather than everywhere, so bottom roughness alone does not explain the observed high drag. In addition, the C_f due to bottom roughness typically has a decreasing trend with increasing water depth (Lentz et al., 2017), opposite to the observed depth dependence, so bottom roughness does not explain the variability of the total C_D with water depth. However, these large-scale bottom features could be an important factor locally, and the combined effects of the multiple scales of bottom roughness on the overall drag still requires further investigation.

5. Discussion

5.1. Explaining the High Drag and its Large Variability

We observed that the effective drag coefficients were greater than expected from bottom friction alone in the North River estuary. Multiple lines of evidence suggest that form drag due to flow separation at channel bends is a leading factor in the high drag observed in the North River. The high values of C_D are consistent with modeling results in sinuous channels with similar geometric parameters in Bo and Ralston (2020), where C_D was dominated by form drag due to flow separation. The correlation between the observed adverse pressure gradients and C_D is also consistent with the explanation that the high C_D is associated with flow separation and form drag. The high C_D shows a flood-ebb asymmetry that is most apparent during high spring tides, which corresponds with a depth dependence of C_D due to higher water levels around max flood. This positive correlation with depth is consistent with the response expected for form drag due to flow separation based on idealized and theoretical models. This suggests that C_D values are higher during flood tides than ebb tides because the deeper water during flood tides leads to stronger flow separation and greater form drag.

Diurnal variations in flood tide C_D appear to correspond with the diurnal inundation of the marsh platform during spring tides and C_D is decreased when the marsh is inundated. As a result, C_D has the opposite trend with water depth when flow is above the channel banks compared with the rest of the data. A potential explanation for this trend is that the local increase in friction with overbank flow inhibits flow separation and reduces the form drag.

The ebb tide C_D has a decreasing trend with river discharge, while the flood tide C_D does not depend on discharge. Stratification increases with river discharge, and the correlation between discharge and ebb C_D may be due to the interaction between the stratification and lateral circulation that results in a local baroclinic pressure gradient that inhibits flow separation. While direct field evidence is lacking, the observations are suggestive that baroclinicity can influence flow separation in estuarine channels. The direct influence of stratification on damping turbulence and reducing drag appears to be less important here, due to the relatively weak stratification during periods with the strongest tidal velocities.

We have focused on the impact of flow separation on the momentum budget, as it creates pressure differences around a bend and results in form drag, but the role of flow separation in the tidal energy flux is still unclear. Flow separation could increase energy loss by enhancing lateral shear dissipation and eddy loss (Chang, 1984) or by narrowing and accelerating the main flow and thereby enhancing bottom dissipation (Bo & Ralston, 2020). $C_{D,energy}$ generally has similar magnitudes to C_D, suggesting that the high energy dissipation is consistent with the high drag. However, the $C_{D,energy}$ calculated based on the channel convergence rate, that is, $L_w = 20$ km, is higher than C_D during most of the observational period (Figure 4b). While uncertainty in the channel geometry estimation could be an explanation, the discrepancy may also relate to differences in how form drag and bottom friction lead to energy loss. Typically the dissipation caused by bottom friction is scaled with the bottom stress times tidal velocity $\|U\|$ (e.g., van Rijn, 2011), but the appropriate velocity for scaling the dissipation associated with form drag is more uncertain (MacCready et al., 2003). The fact that $C_{D,energy}$ (based on $L_w = 20$ km) is higher than C_D from the momentum budget suggests that the effect of form drag in leading to energy dissipation may be overestimated by Equation 13, that is, the dissipation due to form drag needs to be scaled with a smaller velocity than $\|U\|$.

5.2. Other Factors Contributing to the High Drag

While flow separation and form drag appear to play an important role in the high drag observed in the North River, other process may also contribute. Secondary circulation due to curvature and baroclinic forcing is strong in the North River (Kranenburg et al., 2019). Interactions between the secondary circulation and lateral salinity distribution may influence the form drag from flow separation (Section 4.3), but secondary circulation can also directly increase the drag by creating stronger near-bed lateral velocity and by redistributing the streamwise momentum (e.g., Blanckaert & de Vriend, 2003). The near-bottom streamwise velocity ranges between 0.2 and 0.6 m/s at max flood and ebb and the near-bottom lateral velocity is $0 - 0.3$ m/s. The ratio of bottom lateral velocity to streamwise velocity is $0.4 - 0.5$ on average, so based on the quadratic dependence of drag, we can estimate that the lateral velocity may increase the bottom shear stress by $20 - 30\%$. The effects of the redistribution of streamwise momentum by the lateral circulation are harder to estimate. The downward vertical velocity associated with secondary circulation advects greater streamwise velocity toward the bed and squeezes the boundary layer, and the increased velocity variance and thinner boundary layer enhance the local bottom friction. Consequently, secondary circulation can change the bottom stress distribution in channel bends and increase the overall drag.

In addition to flow separation and secondary circulation in channel bends, smaller-scale roughness elements can also influence the drag. The bed roughness features of the midestuary region have been analyzed in Section 4.4, but the integrated effects of multiple scales of bedforms and features like point bars and shallow shoals that can affect the drag still need to be studied. The sharp studied bend does not have a distinct point bar at the apex, nor do other bends in the midestuary region. Shallow bathymetry near the inner bank can enhance local friction and inhibit flow separation, so the absence of a point bar increases the tendency for flow separation in the North River estuary. Kranenburg et al. (2019) suggested that the reversed secondary circulation in this bend, with outward current near the bed, can limit sediment deposition at the inner bank and inhibit the development of a point bar. Flow separation may be another reason for the relatively symmetric cross-channel bathymetric profile at the bend apex. A separation zone near the inner bank restricts the effective channel width at the apex and accelerates flow in the middle channel, and the accelerated velocity can maintain the deep scour at the center of the channel (e.g., Vermeulen et al., 2015). Despite the lack of point bars, several shoals were found in the bends (e.g., Figure 1). These shallow bathymetry features create intermediate-scale roughness in bend flows (larger than bedforms but smaller than bend-scale) and may influence the total drag by affecting the bottom stress, the secondary circulation patterns, or the form drag of flow separation in bends.

Open channel flow literature and engineering guide books typically suggest a drag increase of up to 30% in meanders (e.g., Arcement & Schneider, 1989; Chow, 1959), but observations from the North River estuary indicate that the overall drag increase compared to a straight channel can be much greater. The factors potentially contributing to the high drag in sinuous channels, including flow separation, secondary circulation, and bed forms, require more scientific investigation and engineering evaluation. Incorporation of these processes into numerical models requires either sufficient grid resolution to explicitly represent the complex flow structure or improved drag parameterizations to account for the processes resulting from flow curvature.

6. Conclusion

We observe in an estuary with channel curvature that the drag coefficients are $5 \times 10^{-3} - 20 \times 10^{-3}$, much greater than expected from bottom friction alone. C_D varies at both tidal and seasonal time scales. The C_D values are greater during flood tides than ebb tides, particularly during high spring tides. The tidal asymmetry corresponds with a C_D that increases with water depth. The ebb tide C_D decreases with river discharge but the flood tide C_D shows no dependence on discharge. We observe flow reversal and adverse pressure gradients at the inside of a sharp bend, and the analysis shows that flow separation and the associated form drag is a leading factor in the high total drag. During the highest spring tides, decreased values of C_D were found for overbank flow cases and that is explained by an inhibition of flow separation due to the locally increased friction. Similarly, baroclinic effects during ebbs may inhibit flow separation and explain the decreasing trend with discharge. Other factors may also contribute to the drag, including secondary circulation, multiple scales of bedforms, and shallow shoals, but the various lines of evidence suggest that flow separation plays a key role in the high total drag.

Appendix A: Mean Along-Estuary Momentum Balance

The depth-integrated along-channel momentum equation is (Nihoul & Ronday, 1975)

$$\frac{\partial q}{\partial t} + \frac{\partial}{\partial s}\left(\frac{q^2}{h}\right) = -gh\frac{\partial \eta}{\partial s} - \frac{C_f}{h^2} q\,|q| - \frac{\partial}{\partial s}\int_{-h_0}^{\eta}\int_{z}^{\eta} \beta g S \mathrm{d}z \mathrm{d}z, \tag{A1}$$

where we have neglected wind stress and assumed no bottom slope. q is the depth-integrated flux. h is the total water depth, η is water level, and h_0 is the bathymetry depth. $h = h_0 + \eta$. S is salinity. C_f is the bottom friction coefficient. q is given as

$$q = \int_{\eta-h}^{\eta} u \mathrm{d}z = Uh, \tag{A2}$$

with u being the streamwise velocity and U being the depth average. η is

$$\eta = \overline{\eta} + \eta', \tag{A3}$$

where η' is the measured water level fluctuations and $\overline{\eta}$ is the mean water level that was not directly resolved in the North River observations. We use an overbar to denote time averages of other properties and a prime to denote temporal fluctuations, so

$$q = \overline{q} + q', \tag{A4a}$$

$$U = \overline{U} + U', \tag{A4b}$$

$$h = \overline{h} + \eta', \tag{A4c}$$

$$\overline{h} = h_0 + \overline{\eta} \sim h_0. \tag{A4d}$$

The mean along-estuary momentum balance can be derived by taking the time average of Equation A1, where the unsteady term is zero after averaging and the other three nonlinear terms in Equation A1 can lead to time-mean forcing. Averaging the water level gradient term in Equation A1 gives rise to two terms,

$$\overline{gh\frac{\partial\eta}{\partial s}} = g\overline{h}\frac{\partial\overline{\eta}}{\partial s} + g\overline{\eta'\frac{\partial\eta'}{\partial s}}. \tag{A5}$$

The first term on the right side is the mean barotropic pressure gradient (BTPG or water level gradient forcing), and the second term relates to the tidal stress τ_t.

$$\tau_t = -\rho g\overline{\eta'\frac{\partial\eta'}{\partial s}}. \tag{A6}$$

The tidal stress, as a manifestation of the radiation stress from a tidal wave (Zimmerman, 1978), has been reported in observational studies including on the North Sea (Prandle, 1978) and in San Francisco Bay (Walters & Gartner, 1985). Rearranging Equation A6 and assuming sinusoidal tides,

$$\tau_t = -\frac{1}{2}\rho g\frac{\partial\overline{(\eta'^2)}}{\partial s} = -\frac{1}{4}\rho g\frac{\partial}{\partial s}(\|\eta\|^2), \tag{A7}$$

where $\|\eta\|$ is the norm of tidal water level fluctuation, that is, tidal amplitude.

Averaging the advection term in Equation A1, we get

$$\frac{\partial}{\partial s}\overline{\left(\frac{q^2}{h}\right)} \sim \frac{1}{h}\frac{\partial}{\partial s}\overline{(q'^2)}. \tag{A8}$$

The mean forcing associated with the advection term is generally small. Moreover, velocity is nonuniform laterally due to bathymetry variation and channel curvature, so the along-channel flux gradient based on measurements at a single location in the North River estuary is not representative for use in this estimate. Therefore, we have neglected this advection term in the mean momentum balance.

The average of the frictional term in Equation A1 represents the friction of the mean flow, which consists of the freshwater discharge and the Eulerian return flow of the landward Stokes drift of the tidal wave (Uncles & Jordan, 1980; Zimmerman, 1979). For estuaries with small or moderate discharge (e.g., the North River estuary), $\overline{U} \ll \|U\|$, where $\|U\|$ is the norm of tidal velocity U'. The mean flow friction $\tau_{b,\overline{u}}$ can thus be estimated as (e.g., Parker, 2007)

$$\tau_{b,\overline{u}} = -\overline{\frac{C_f}{h^2}\rho q\,|q|} = -\overline{C_f\rho U\,|U|} = -\frac{4}{\pi}C_f\rho\,\|U\|\,\overline{U}. \tag{A9}$$

Averaging the salinity gradient term in Equation A1 yields the mean baroclinic pressure gradient (BCPG) forcing

$$-\overline{\frac{\partial}{\partial s}\int_{-h_0}^{\eta}\int_{z}^{\eta}\beta gS\mathrm{d}z\mathrm{d}z} \approx -\overline{\frac{1}{2}\beta gh^2\frac{\partial\langle S\rangle}{\partial s}} \approx -\overline{\frac{1}{2}\beta gh\frac{\partial\langle S\rangle}{\partial s}}\overline{h}, \tag{A10}$$

where $\langle S\rangle$ is the depth-averaged salinity.

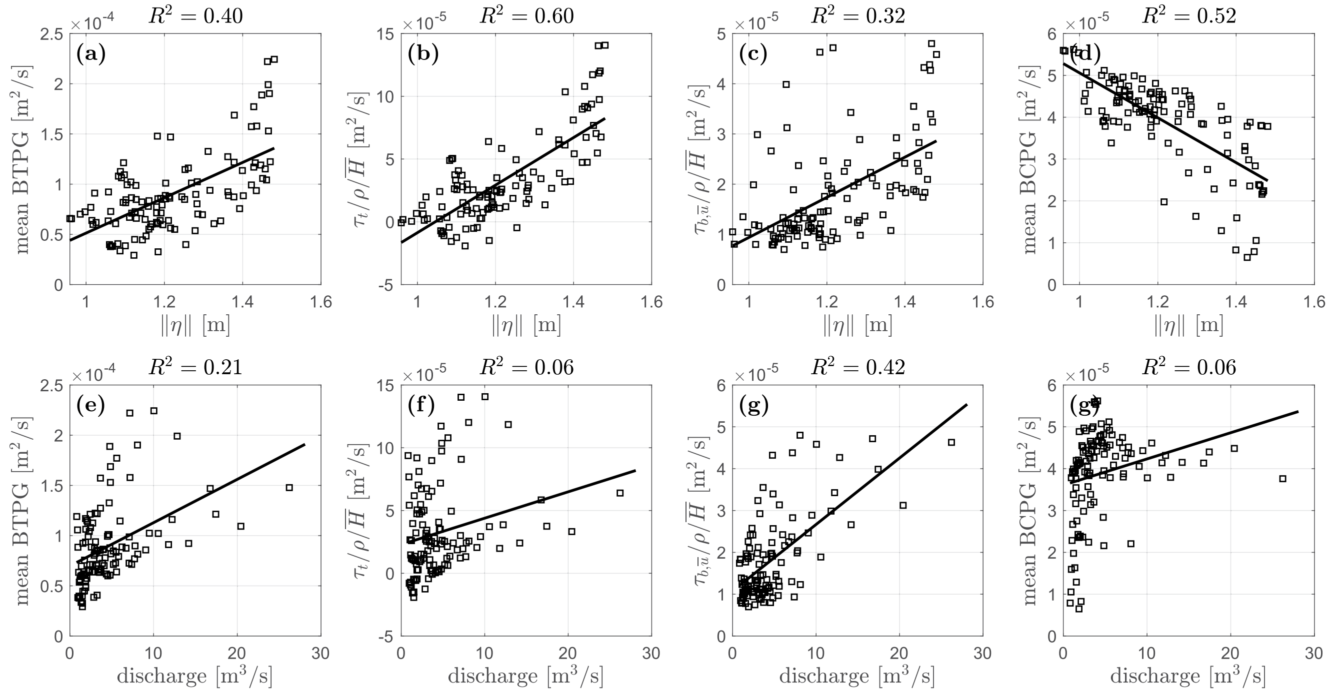

Figure A1. Correlation between the mean barotropic pressure gradient (BTPG), τ_t, $\tau_{b,\overline{u}}$, the mean baroclinic pressure gradient (BCPG), and tidal amplitude, river discharge.

Therefore, in the mean momentum budget, the mean BTPG is balanced with three terms, the tidal stress τ_t, the mean flow friction $\tau_{b,\overline{u}}$, and the mean BCPG. The mean BTPG can be estimated as

$$g\frac{\partial \overline{\eta}}{\partial s} = \frac{1}{\rho \overline{h}}\left(\tau_t + \tau_{b,\overline{u}}\right) - \overline{\frac{1}{2}\beta g h \frac{\partial \langle S \rangle}{\partial s}}, \tag{A11}$$

where τ_t and $\tau_{b,\overline{u}}$ are given by Equations A7 and A9. We have compared the estimation from Equation A11 with the mean BTPG in model results from Bo and Ralston (2020) and found that the estimation agrees well ($R^2 = 0.85$).

We calculated τ_t, $\tau_{b,\overline{u}}$, and the mean BCPG from the observations in the North River estuary (Section 2.3.2) and examined their dependence on tides and discharge (Figure A1). τ_t is primarily dependent on tides, and as the tidal amplitude increases, the tidal decay rate increases and the tidal stress becomes stronger. Freshwater discharge creates the mean river flow and tides can lead to a return flow, and therefore, $\tau_{b,\overline{u}}$ is correlated with both discharge and tidal amplitude. The mean BCPG has a negative correlation with tidal amplitude and a weak positive dependence on discharge.

Data Availability Statement

Data supporting this study are available online (at https://doi.org/10.5281/zenodo.4540332).

Acknowledgments
The authors thank Adrian Mikhail P. Garcia and Jay Sisson for field work assistance and two anonymous reviewers for insightful comments. The research leading to these results was funded by NSF awards OCE-1634480, OCE-1634481, and OCE-2123002.

References

Arcement, G. J., & Schneider, V. R. (1989). *Guide for selecting Manning's roughness coefficients for natural channels and flood plains*. US Government Printing Office. https://doi.org/10.3133/wsp2339

Blanckaert, K. (2010). Topographic steering, flow recirculation, velocity redistribution, and bed topography in sharp meander bends. *Water Resources Research*, *46*(9). https://doi.org/10.1029/2009wr008303

Blanckaert, K. (2015). Flow separation at convex banks in open channels. *Journal of Fluid Mechanics*, *779*, 432–467. https://doi.org/10.1017/jfm.2015.397

Blanckaert, K., & de Vriend, H. J. (2003). Nonlinear modeling of mean flow redistribution in curved open channels. *Water Resources Research*, *39*(12). https://doi.org/10.1029/2003wr002068

Blanckaert, K., & Graf, W. H. (2004). Momentum transport in sharp open-channel bends. *Journal of Hydraulic Engineering*, *130*(3), 186–198. https://doi.org/10.1061/(asce)0733-9429(2004)130:3(186)

Blanckaert, K., Kleinhans, M. G., McLelland, S. J., Uijttewaal, W. S., Murphy, B. J., van de Kruijs, A., et al. (2013). Flow separation at the inner (convex) and outer (concave) banks of constant-width and widening open-channel bends. *Earth Surface Processes and Landforms*, *38*(7), 696–716. https://doi.org/10.1002/esp.3324

Bo, T., & Ralston, D. K. (2020). Flow separation and increased drag coefficient in estuarine channels with curvature. *Journal of Geophysical Research: Oceans*, *125*, e2020JC016267. https://doi.org/10.1029/2020jc016267

Bowden, K., & Fairbairn, L. (1956). Measurements of turbulent fluctuations and Reynolds stresses in a tidal current. *Proceedings of the Royal Society of London - Series A: Mathematical and Physical Sciences*, *237*(1210), 422–438. https://doi.org/10.1098/rspa.1956.0188

Bricker, J. D., Inagaki, S., & Monismith, S. G. (2005). Bed drag coefficient variability under wind waves in a tidal estuary. *Journal of Hydraulic Engineering*, *131*(6), 497–508. https://doi.org/10.1061/(asce)0733-9429(2005)131:6(497)

Chang, H. H. (1983). Energy expenditure in curved open channels. *Journal of Hydraulic Engineering*, *109*(7), 1012–1022. https://doi.org/10.1061/(asce)0733-9429(1983)109:7(1012)

Chang, H. H. (1984). Variation of flow resistance through curved channels. *Journal of Hydraulic Engineering*, *110*(12), 1772–1782. https://doi.org/10.1061/(asce)0733-9429(1984)110:12(1772)

Chant, R. J. (2002). Secondary circulation in a region of flow curvature: Relationship with tidal forcing and river discharge. *Journal of Geophysical Research*, *107*(C9), 1–11. https://doi.org/10.1029/2001jc001082

Chow, V. T. (1959). *Open-channel hydraulics* (p. 680). McGraw-Hill.

Dietrich, W. E., & Smith, J. D. (1983). Influence of the point bar on flow through curved channels. *Water Resources Research*, *19*(5), 1173–1192. https://doi.org/10.1029/wr019i005p01173

Dronkers, J. J. (1964). *Tidal computations in rivers and coastal waters*. Amsterdam: North-Holland Publishing Company.

Ferguson, R. I., Parsons, D. R., Lane, S. N., & Hardy, R. J. (2003). Flow in meander bends with recirculation at the inner bank. *Water Resources Research*, *39*(11), 299–13. https://doi.org/10.1029/2003wr001965

Finotello, A., Ghinassi, M., Carniello, L., Belluco, E., Pivato, M., Tommasini, L., & D'Alpaos, A. (2020). Three-dimensional flow structures and morphodynamic evolution of microtidal meandering channels. *Water Resources Research*, *56*(7), e2020WR027822. https://doi.org/10.1029/2020wr027822

Fong, D. A., Monismith, S. G., Stacey, M. T., & Burau, J. R. (2009). Turbulent stresses and secondary currents in a tidal-forced channel with significant curvature and asymmetric bed forms. *Journal of Hydraulic Engineering*, *135*(3), 198–208. https://doi.org/10.1061/(asce)0733-9429(2009)135:3(198)

Geyer, W. R. (1993). The importance of suppression of turbulence by stratification on the estuarine turbidity maximum. *Estuaries*, *16*(1), 113–125. https://doi.org/10.2307/1352769

Geyer, W. R. (2010). Estuarine salinity structure and circulation. *Contemporary issues in estuarine physics* (pp. 12–26).

Geyer, W. R., Trowbridge, J. H., & Bowen, M. M. (2000). The dynamics of a partially mixed estuary. *Journal of Physical Oceanography*, *30*(8), 2035–2048. https://doi.org/10.1175/1520-0485(2000)030<2035:tdoapm>2.0.co;2

Grant, W. D., & Madsen, O. S. (1982). Movable bed roughness in unsteady oscillatory flow. *Journal of Geophysical Research*, *87*(C1), 469–481. https://doi.org/10.1029/jc087ic01p00469

Grant, W. D., & Madsen, O. S. (1986). The continental-shelf bottom boundary layer. *Annual Review of Fluid Mechanics*, *18*(1), 265–305. https://doi.org/10.1146/annurev.fl.18.010186.001405

Gross, E. S., Koseff, J. R., & Monismith, S. G. (1999). Three-dimensional salinity simulations of South San Francisco Bay. *Journal of Hydraulic Engineering*, *125*(11), 1199–1209. https://doi.org/10.1061/(asce)0733-9429(1999)125:11(1199)

Heathershaw, A., & Simpson, J. (1978). The sampling variability of the Reynolds stress and its relation to boundary shear stress and drag coefficient measurements. *Estuarine and Coastal Marine Science*, *6*(3), 263–274. https://doi.org/10.1016/0302-3524(78)90015-4

James, C., Liu, W., & Myers, W. (2001). Conveyance of meandering channels with marginal vegetation. *Proceedings of the Institution of Civil Engineers-Water and Maritime Engineering*, *148*(2), 97–106. https://doi.org/10.1680/wame.2001.148.2.97

Jamieson, E. C., Ruta, M. A., Rennie, C. D., & Townsend, R. D. (2013). Monitoring stream barb performance in a semi-alluvial meandering channel: Flow field dynamics and morphology. *Ecohydrology*, *6*(4), 611–626. https://doi.org/10.1002/eco.1370

Kadlec, R. H. (1990). Overland flow in wetlands: Vegetation resistance. *Journal of Hydraulic Engineering*, *116*(5), 691–706. https://doi.org/10.1061/(asce)0733-9429(1990)116:5(691)

Kaimal, J. C., Wyngaard, J., Izumi, Y., & Coté, O. (1972). Spectral characteristics of surface-layer turbulence. *Quarterly Journal of the Royal Meteorological Society*, *98*(417), 563–589. https://doi.org/10.1002/qj.49709841707

Kalkwijk, J. P. T., & Booij, R. (1986). Adaptation of secondary flow in nearly-horizontal flow. *Journal of Hydraulic Research*, *24*(1), 19–37. https://doi.org/10.1080/00221688609499330

Kimball, P., Bailey, J., Das, S., Geyer, R., Harrison, T., Kunz, C., et al. (2014). The WHOI Jetyak: An autonomous surface vehicle for oceanographic research in shallow or dangerous waters. *IEEE/OES autonomous underwater vehicles (AUV)*. (pp. 1–7). IEEE. https://doi.org/10.1109/auv.2014.7054430

Kranenburg, W. M., Geyer, W. R., Garcia, A. M. P., & Ralston, D. K. (2019). Reversed lateral circulation in a sharp estuarine bend with weak stratification. *Journal of Physical Oceanography*, *49*, 1619–1637. https://doi.org/10.1175/jpo-d-18-0175.1

Lacy, J. R., & Monismith, S. G. (2001). Secondary currents in a curved, stratified, estuarine channel. *Journal of Geophysical Research*, *106*(C12), 31283–31302. https://doi.org/10.1029/2000jc000606

Leeder, M. R., & Bridges, P. H. (1975). Flow separation in meander bends. *Nature*, *253*, 1–2. https://doi.org/10.1038/253338a0

Lentz, S. J., Davis, K. A., Churchill, J. H., & DeCarlo, T. M. (2017). Coral reef drag coefficients–water depth dependence. *Journal of Physical Oceanography*, *47*(5), 1061–1075. https://doi.org/10.1175/jpo-d-16-0248.1

Leopold, L. B. (1960). *Flow resistance in sinuous or irregular channels* (p. 24). US Government Printing Office.

Leopold, L. B., & Wolman, M. G. (1960). River meanders. The *Geological Society of America Bulletin*, *71*(6), 769–793. https://doi.org/10.1130/0016-7606(1960)71[769:rm]2.0.co;2

Lewis, R., & Lewis, J. (1987). Shear stress variations in an estuary. *Estuarine, Coastal and Shelf Science*, *25*(6), 621–635. https://doi.org/10.1016/0272-7714(87)90011-4

MacCready, P., Pawlak, G., Edwards, K., & McCabe, R. (2003). Form drag on ocean flows. *Near boundary processes and their parameterization: Proc 13th'Aha Huliko'a Hawaiian winter workshop* (pp. 119–130).

Marani, M., Lanzoni, S., Zandolin, D., Seminara, G., & Rinaldo, A. (2002). Tidal meanders. *Water Resources Research*, *38*(11), 7–14. https://doi.org/10.1029/2001wr000404

Marriott, M. J. (1998). *Hydrodynamics of flow around bends in meandering and compound channelsPhD thesis*. University of Herfordshire.

McCabe, R. M., MacCready, P., & Pawlak, G. (2006). Form drag due to flow separation at a headland. *Journal of Physical Oceanography*, *36*(11), 2136–2152. https://doi.org/10.1175/jpo2966.1

Monismith, S. G., Hirsh, H., Batista, N., Francis, H., Egan, G., & Dunbar, R. B. (2019). Flow and drag in a seagrass bed. *Journal of Geophysical Research: Oceans*, *124*(3), 2153–2163. https://doi.org/10.1029/2018jc014862

Nanson, R. A. (2010). Flow fields in tightly curving meander bends of low width-depth ratio. *Earth Surface Processes and Landforms: The Journal of the British Geomorphological Research Group*, *35*(2), 119–135.

Nepf, H. (1999). Drag, turbulence, and diffusion in flow through emergent vegetation. *Water Resources Research*, *35*(2), 479–489. https://doi.org/10.1029/1998wr900069

Nidzieko, N. J., Hench, J. L., & Monismith, S. G. (2009). Lateral circulation in well-mixed and stratified estuarine flows with curvature. *Journal of Physical Oceanography*, *39*(4), 831–851. https://doi.org/10.1175/2008jpo4017.1

Nihoul, J. C., & Ronday, F. C. (1975). The influence of the "tidal stress" on the residual circulation. *Tellus*, *27*(5), 484–490. https://doi.org/10.3402/tellusa.v27i5.10174

Parker, B. B. (2007). *Tidal analysis and prediction*. NOAA Special Publication.

Pein, J., Valle-Levinson, A., & Stanev, E. V. (2018). Secondary circulation asymmetry in a meandering, partially stratified estuary. *Journal of Geophysical Research: Oceans*, *123*(3), 1670–1683. https://doi.org/10.1002/2016jc012623

Prandle, D. (1978). Residual flows and elevations in the southern North Sea. *Proceedings of the Royal Society of London. A. Mathematical and Physical Sciences*, *359*(1697), 189–228. https://doi.org/10.1098/rspa.1978.0039

Rogers, J. S., Maticka, S. A., Chirayath, V., Woodson, C. B., Alonso, J. J., & Monismith, S. G. (2018). Connecting flow over complex terrain to hydrodynamic roughness on a coral reef. *Journal of Physical Oceanography*, *48*(7), 1567–1587. https://doi.org/10.1175/jpo-d-18-0013.1

Schnauder, I., & Sukhodolov, A. (2012). Flow in a tightly curving meander bend: Effects of seasonal changes in aquatic macrophyte cover. *Earth Surface Processes and Landforms*, *37*(11), 1142–1157. https://doi.org/10.1002/esp.3234

Seim, H., Blanton, J., & Elston, S. (2006). Tidal circulation and energy dissipation in a shallow, sinuous estuary. *Ocean Dynamics*, *56*(3–4), 360–375. https://doi.org/10.1007/s10236-006-0078-x

Seim, H. E., Blanton, J. O., & Gross, T. (2002). Direct stress measurements in a shallow, sinuous estuary. *Continental Shelf Research*, *22*(11–13), 1565–1578. https://doi.org/10.1016/s0278-4343(02)00029-8

Seim, H. E., & Gregg, M. C. (1997). The importance of aspiration and channel curvature in producing strong vertical mixing over a sill. *Journal of Geophysical Research*, *102*(C2), 3451–3472. https://doi.org/10.1029/96jc03415

Signell, R. P., & Geyer, W. R. (1991). Transient eddy formation around headlands. *Journal of Geophysical Research*, *96*(C2), 2561–2575. https://doi.org/10.1029/90jc02029

Soulsby, R. (1990). In B. Le Méhauté (Ed.), *Tidal current boundary layers, the sea, part 1*. University of MiamiJohn Wiley & Sons Inc.

Soulsby, R. (1997). *Dynamics of marine sands* (p. 249). Telford.

Sternberg, R. (1968). Friction factors in tidal channels with differing bed roughness. *Marine Geology*, *6*(3), 243–260. https://doi.org/10.1016/0025-3227(68)90033-9

Tennekes, H., Lumley, J. L. (1972). *A first course in turbulence*. MIT press.

Thomson, J. (1877). V. on the origin of windings of rivers in alluvial plains, with remarks on the flow of water round bends in pipes. *Proceedings of the Royal Society of London*, *25*(171–178). 5–8. https://doi.org/10.1098/rspl.1876.0004

Trowbridge, J. H., & Lentz, S. J. (2018). The bottom boundary layer. *Annual Review of Marine Science*, *10*, 397–420. https://doi.org/10.1146/annurev-marine-121916-063351

Uncles, R., & Jordan, M. (1980). A one-dimensional representation of residual currents in the Severn estuary and associated observations. *Estuarine and Coastal Marine Science*, *10*(1), 39–60. https://doi.org/10.1016/s0302-3524(80)80048-x

van Rijn, L. C. (2011). Analytical and numerical analysis of tides and salinities in estuaries; part i: Tidal wave propagation in convergent estuaries. *Ocean Dynamics*, *61*(11), 1719–1741. https://doi.org/10.1007/s10236-011-0453-0

Vermeulen, B., Hoitink, A., & Labeur, R. (2015). Flow structure caused by a local cross-sectional area increase and curvature in a sharp river bend. *Journal of Geophysical Research: Earth Surface*, *120*(9), 1771–1783. https://doi.org/10.1002/2014jf003334

Walters, R. A., & Gartner, J. W. (1985). Subtidal sea level and current variations in the northern reach of San Francisco Bay. *Estuarine, Coastal and Shelf Science*, *21*(1), 17–32. https://doi.org/10.1016/0272-7714(85)90003-4

Zimmerman, J. (1978). Topographic generation of residual circulation by oscillatory (tidal) currents. *Geophysical & Astrophysical Fluid Dynamics*, *11*(1), 35–47. https://doi.org/10.1080/03091927808242650

Zimmerman, J. (1979). On the euler-Lagrange transformation and the stokes' drift in the presence of oscillatory and residual currents. *Deep Sea Research Part A. Oceanographic Research Papers*, *26*(5), 505–520. https://doi.org/10.1016/0198-0149(79)90093-1